

## Article

# Characterization of Bentonites from the *In Situ* ABM5 Heater Experiment at Äspö Hard Rock Laboratory, Sweden

Ana María Fernández <sup>1,\*</sup> , José F. Marco <sup>2</sup> , Paula Nieto <sup>1</sup> , Fco. Javier León <sup>1</sup>, Luz María Robredo <sup>1</sup>,  
María Ángeles Clavero <sup>1</sup>, Ana Isabel Cardona <sup>1</sup>, Sergio Fernández <sup>1</sup>, Daniel Svensson <sup>3</sup> and Patrik Sellin <sup>3</sup>

<sup>1</sup> CIEMAT, Centro de Investigaciones Energéticas, Medioambientales y Tecnológicas, Departamento de Medio Ambiente, 28040 Madrid, Spain; paul.nch@gmail.com (P.N.); fcojavier.leon@ciemat.es (F.J.L.); l.robredo@ciemat.es (L.M.R.); ma.clavero@ciemat.es (M.Á.C.); anaisabel.cardona@ciemat.es (A.I.C.); sergio.fernandez@ciemat.es (S.F.)

<sup>2</sup> CSIC, Consejo Superior de Investigaciones Científicas, Instituto de Química Física “Rocasolano”, 28006 Madrid, Spain; jfmarco@iqfr.csic.es

<sup>3</sup> Department of Research and Safety Assessment, SKB—Svensk Kärnbränslehantering, SE-57229 Oskarshamn, Sweden; daniel.svensson@skb.se (D.S.); patrik.sellin@skb.se (P.S.)

\* Correspondence: anamaria.fernandez@ciemat.es

**Abstract:** The Alternative Buffer Material ABM5 experiment is an *in situ* medium-scale experiment performed at Äspö Hard Rock Laboratory (HRL) conducted by SKB in Sweden with the aim of analysing the long-term stability of bentonites used as an engineering barrier for a high-level radioactive waste repository (HLWR). In this work, four different ring-shaped Ca- and Na-bentonite blocks, which were piled around a carbon steel cylindrical heater, subjected to a maximum temperature of 250 °C and hydrated with saline Na-Ca-Cl Äspö groundwater (0.91 ionic strength), were characterized after dismantling. This work allowed us to identify the main geochemical processes involved, as well as the modifications in the physico-chemical properties and pore water composition after 4.4 years of treatment. No significant modifications in mineralogy were observed in samples close to the heater contact, except an increase in Fe content due to C-steel corrosion, carbonate dissolution/precipitation (mainly calcite and siderite) and Mg increase. No magnetite and a low amount of Fe(II) inside the clay mineral structure were detected. No modifications were observed in the smectite structure, except a slight increase in total and tetrahedral charge. A decrease in external surface area and cation exchange capacity (CEC) was found in all samples, with lower values being detected at the heater contact. As a consequence of the diffusion of the infiltrating groundwater, a modification of the composition at clay mineral exchange sites occurred. Ca-bentonites increased their Na content at exchange sites, whereas Na-bentonite increased their Ca content. Exchangeable Mg content decreased in all bentonites, except in MX-80 located at the bottom part of the package. A salinity gradient is observed through the bentonite blocks from the granite to the heater contact due to anions are controlled by diffusion and anion exclusion. The pore water chemistry of bentonites evolved as a function of the diffusion transport of the groundwater, the chemical equilibrium of cations at exchange sites and mineral dissolution/precipitation processes. These reactions are in turn dependent on temperature and water vapor fluxes.

**Keywords:** bentonites; smectites; pore water chemistry; mineralogy; cation exchange; ABM experiment; large-scale tests



**Citation:** Fernández, A.M.; Marco, J.F.; Nieto, P.; León, F.J.; Robredo, L.M.; Clavero, M.Á.; Cardona, A.I.; Fernández, S.; Svensson, D.; Sellin, P. Characterization of Bentonites from the *In Situ* ABM5 Heater Experiment at Äspö Hard Rock Laboratory, Sweden. *Minerals* **2022**, *12*, 471. <https://doi.org/10.3390/min12040471>

Academic Editor: Huaming Yang

Received: 28 February 2022

Accepted: 8 April 2022

Published: 12 April 2022

**Publisher’s Note:** MDPI stays neutral with regard to jurisdictional claims in published maps and institutional affiliations.



**Copyright:** © 2022 by the authors. Licensee MDPI, Basel, Switzerland. This article is an open access article distributed under the terms and conditions of the Creative Commons Attribution (CC BY) license (<https://creativecommons.org/licenses/by/4.0/>).

## 1. Introduction

Bentonites are essential in the long-term safety of the multi-barrier system for the disposal of nuclear wastes. The efficiency of the bentonite engineered barrier system (EBS) is based on its confinement properties: swelling capacity, low permeability, low diffusivity and high radionuclide retention. Consequently, it is important to have confidence and

demonstrate the preservation of these properties under real repository conditions over hundreds of thousands of years [1].

Predicting long-term bentonite barrier behaviour is usually undertaken using results from experiments operated in underground research laboratories (URL) in real conditions, at a real scale and for long test times: Meuse/Haute-Marne in France, HADES in Belgium, Äspö in Sweden, Mont Terri and Grimsel in Switzerland. Different *in situ* large-scale EBS experiments have been accomplished since 1989 by using both compacted bentonite (e.g., prototype, FEBEX, TBT and LOT *in situ* tests) and high-density bentonite pellets (e.g., FE, RESEAL and EB experiments) (see [2] for references). The aim was to analyse the manufacturing, handling, properties and long-term performance of the bentonite materials (e.g., [3,4] and references therein).

The Alternative Buffer Material (ABM) experiment is a medium-scale field experiment performed at Äspö Hard Rock Laboratory (HRL) in Sweden with the aim of analysing the long-term stability of different bentonites under similar conditions of the current Swedish concept for a high-level radioactive waste repository (HLWR), and under adverse conditions regarding temperature. The test, conducted by SKB (Swedish Nuclear Fuel and Waste Management Company), is based on the KBS-3 (kärnbränslesäkerhet, nuclear fuel safety) concept, in which a repository is placed at approximately 500 m depth in crystalline rock, and a buffer of compacted clay surrounds corrosion-resistant copper canisters containing the waste, in order to minimize water flow and radionuclide transport to the granite host rock [5].

The ABM experiment includes six medium-scale test packages, each one consisting of a central carbon steel tube with heaters, and a buffer of compacted clay artificially hydrated with natural Äspo granitic groundwater for rapid water saturation. Eleven different clays were chosen for the buffers to examine the effects of smectite content, interlayer cations and overall iron content. In addition, bentonite pellets with different proportions of quartz are being tested in some tests. The main purposes of the project were to characterize and compare different bentonite qualities and to identify any differences in behaviour or long-term stability of hydro-mechanical properties, mineralogy and chemical composition after groundwater saturation, heating and interaction with corroding metals (iron–bentonite interactions) [5].

The buffer in package 1 (2006–2009) and package 2 (2006–2013) was subjected to artificial wetting and heating for 28 months and 6.5 years, respectively; the maximum temperatures were 130 °C during the last year for package 1 (ABM1) and 141 °C after the first 2.5 years for package 2 (ABM2). The ABM45 project started in 2012, including three new packages (4, 5 and 6). The ABM5 experiment ran from 2012 to 2017. ABM5 represents an adverse scenario of an HLWR repository, since it is one of the hottest bentonite tests (up to 250 °C) conducted in an underground research laboratory to date (URL). ABM3 (2006–), ABM4 (2012–) and ABM6 (2012–) are still running and are expected to be excavated in 2024.

After the experiments, the buffer packages ABM1, ABM2 and ABM5 were retrieved and analysed, with the studies being focused on hydromechanical properties [5], geochemical and mineralogical alteration [5–9], cation exchange rearrangements [10,11], and redox chemistry evolution [12–14]. However, few studies have been performed on the pore water chemistry in these systems [15].

The aim of this work is to analyse the geochemical processes observed in some bentonite samples obtained after dismantling the ABM5 *in situ* experiment, with special emphasis on pore water chemistry studies. The dismantling of this test allowed us to quantify the alteration of the bentonites properties due to different types of perturbations: (a) interactions with artificial granitic groundwater (saturation phase), (b) heat (boiling and desaturation phase due to heating), and (c) interactions with the allochthonous engineered materials (metals, concrete, organics, etc.).

## 2. Materials and Methods

### 2.1. ABM5 Experiment

The project Alternative Buffer Materials 45 (ABM45) was a field experiment consisting of three packages: 4, 5 and 6, each one containing 30 ring-shaped bentonite blocks piled around a cylindrical tube made of carbon steel P235TR1 (Table 1, Figure 1). An electrical heater of 1000 W was placed inside the tube as a heat source. The packages were installed in boreholes (30 cm diameter and 3 m depth) drilled in the tunnel named T ASD at ca. 420 m depth in the Äspö Hard Rock Laboratory [16]. The granitic host rock consisted of Äspö diorite and greenstone.

**Table 1.** Chemical composition in wt.% of carbon steel (steel grade P235TR1): EN 10216-1-2014.

Element	Fe	C	Si	Mn	P	S	Cr	Mo	Ni	Cu	Nb	Ti	V
maximum	ball	0.16	0.35	1.20	0.025	0.02	0.30	0.08	0.30	0.30	0.01	0.04	0.02

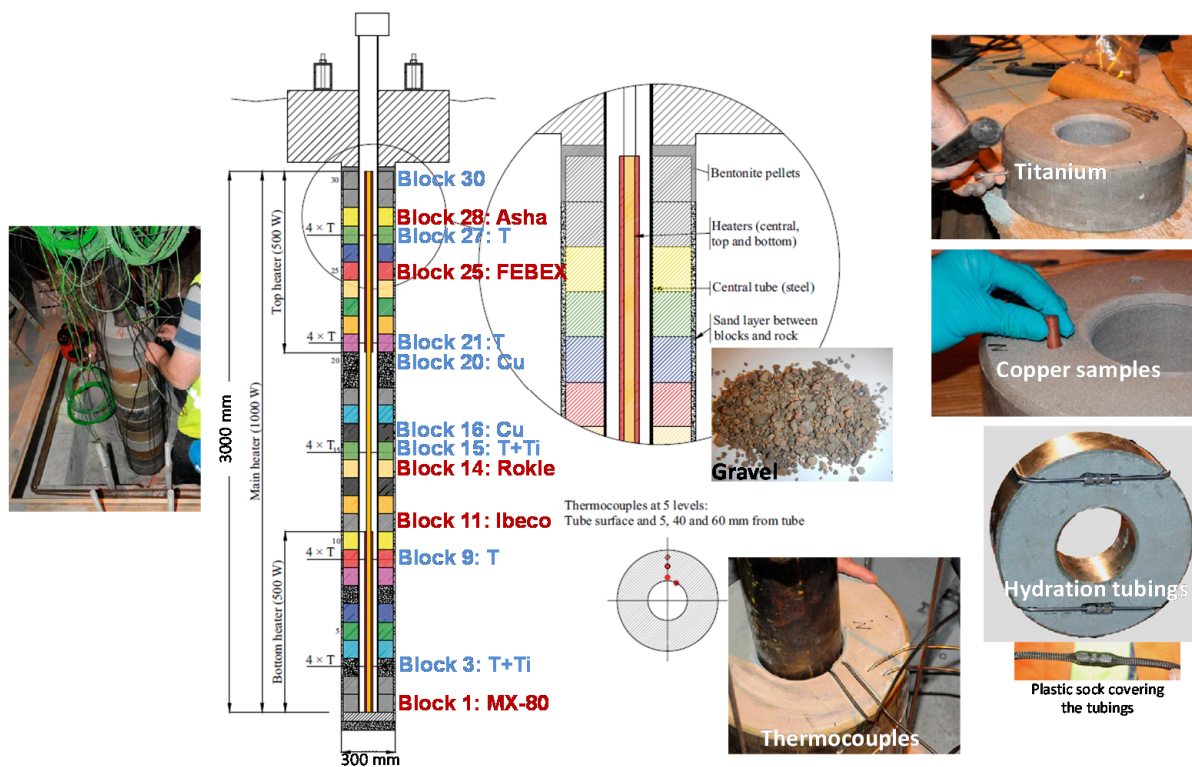


**Figure 1.** Schematic design of the ABM5 test package (after [16], courtesy of SKB). In red: samples analysed in this study. In blue: block containing thermocouples and Cu and Ti coupons. Colours represent different types of bentonites.

The package 5 (ABM5 experiment) was deposited in the borehole named KD0098G01, where there was a groundwater inflow of around 8.5 L/d, coming from a fracture located −0.8 m. However, an artificial water saturation system was used for a rapid saturation of the bentonite. The heating test duration was 4.4 years, starting on 15 November 2012 and finishing on 10 April 2017. The bentonite was heated to 50 °C for the first three and half years, to support saturation and prevent water boiling, and then in 2016 the temperature was increased stepwise to 150 °C and up to 250 °C at the bentonite/heater interface for approximately the last six months of exposure (Figure 2). Estimated maximum temperatures at the heater contact of 240–250 °C were reached between blocks 22 and 8, with decreasing temperatures both at bottom and top part of the bentonite column (<188–156 °C, blocks 3 and 27), and as a function of the granite contact (Figure 2). In the hottest blocks,

temperatures of more than 150 °C were reached at a distance of 6 cm from the heater, with the thickness of the bentonite block being 10 cm (see also [8,9]).

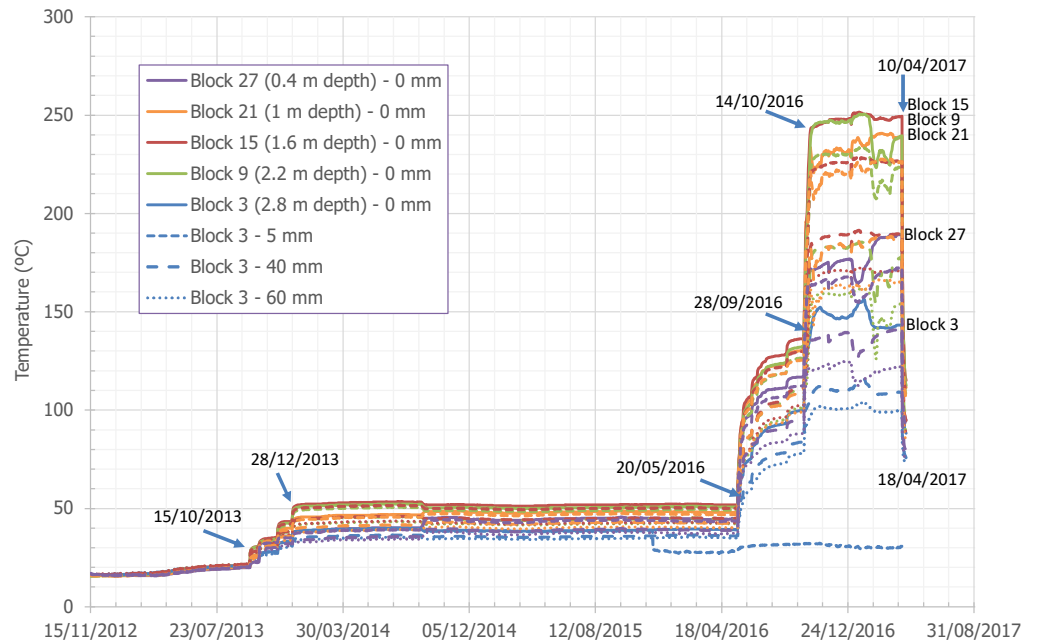


**Figure 2.** Temperatures profiles as a function of the heater contact (0, 5, 40 and 60 mm) measured by thermocouples inside bentonite blocks n° 3, 9 (Asha NW BFL-L), 15 (MX-80), 21 (Kunigel) and 27 (Calcigel).

The bentonites selected for this experiment were of 12 types [16]: MX-80 2012 (Blocks 30, 29, 20, 15, 8, 2, 1), Asha 505 2011 (Blocks 28,16), Asha NW BFL-L (Blocks 19, 9, 3), Deponit CA-N (26, 4), Febex 2012 (Blocks 25, 13), Ikosorb 2011 (Blocks 22, 7), Rokle 2012 (Blocks 18, 14), Kunigel V1 (Blocks 21, 5), GMZ 2011 (Blocks 24, 6), Saponite 2012 (Blocks 17, 12), Calcigel 2012 (Blocks 27, 10) and Ibeco SEAL M-90, old batch (Blocks 23, 11). At least two blocks of each bentonite were placed in the test, except for MX-80 and Asha NW BFL-L, for which 5 and 3 blocks were set, respectively. Therefore, 28 bentonite blocks as compacted rings penetrated by the heater were placed inside the test borehole. Additional MX-80 blocks (#1 and #30) were positioned at the top and bottom to secure a tight sealing. After installation of the test package, concrete plugs were casted above the test borehole in order to prevent the bentonite from swelling upwards.

The ring-shaped blocks (~27.73 cm outer diameter, ~11.0 cm inner diameter and 10 cm height) were compacted uniaxially in a special mould with a pressure between 50 and 100 MPa. A thin layer of molybdenum sulfide containing grease was applied on all steel surfaces in contact with the bentonite powder in order to lubricate to decrease friction. The grease was removed mechanically from the blocks surfaces prior to the bentonites be installed in the test [16].

The outermost gap between bentonite blocks and rock was filled with gravel (2–80 mm), in which 6 mm-diameter titanium tubes with small holes, covered by a plastic sleeve, were placed for a rapid saturation of the bentonite using an artificial groundwater (Table 2). The initial water content of the compacted bentonite was that of “as-received” air dried material. The dry density of the blocks installed in 2013 is listed in Table 3.

**Table 2.** Main composition of the Äspö Groundwater from water supply borehole KA2598A [5].

Ion	Water-Type	I (M)	Na	K	Ca	Mg	HCO <sub>3</sub> <sup>-</sup>	Cl <sup>-</sup>	SO <sub>4</sub> <sup>2-</sup>	Br <sup>-</sup>	F <sup>-</sup>	Si	pH
mg/L	Ca-Na-Cl	0.91	2470	12.4	2560	64.8	51.7	8580	483	59	1.5	6.3	7.33

**Table 3.** Average physical properties from bentonite blocks analysed at CIEMAT prior to (initial) and after 4.4 years of test (final).

Sample	Depth (m)	Max. Temp. (°C) <sup>4</sup>	Bentonite Mass (g)	Water Content w.c. (%)		Dry Density (g/cm <sup>3</sup> )		Grain Density (g/cm <sup>3</sup> ) <sup>2</sup>	Porosity (%)		Degree of Saturation (%)		Water Content at Saturation (%)
				Initial <sup>1</sup>	Final <sup>3</sup>	Initial <sup>1</sup>	Final <sup>3</sup>		Initial	Final	Initial	Final	Final
Asha Block 28	0.3	187.0	10,820	13.1	30.1	1.84	1.49	2.869	36	48	67.3	93.0	32.4
FEBEX Block 25	0.6	216.5	10,640	14.3	27.9	1.80	1.51	2.735	34	45	75.2	94.1	29.7
Rokle Block 14	1.7	252.6	10,800	17.2	29.0	1.80	1.60	2.940	39	46	80.3	102.2	28.4
IBECO Block 11	2.0	255.1	10,740	14.7	32.0	1.86	1.50	2.753	33	45	83.6	106.0	30.2
MX-80 Block 1	3.0	155.0	11,040	10.6	31.1	1.93	1.49	2.735	29	46	69.9	101.7	30.6

<sup>1</sup> [16]; <sup>2</sup> [5]; <sup>3</sup> Average values; <sup>4</sup> Estimated from thermocouples measurements.

The ABM45 experiments were sparsely instrumented (Figure 1). Twenty thermocouples type T (Chromel-alumel with a shield of cupronickel, 4.5 mm diameter) were installed in blocks numbers 3, 9, 15, 21 and 27. Four thermocouples were installed at each level in pre-drilled holes in the bentonite rings, one on the steel surface and three in the buffer at a radial distance from the heater (5, 40 and 60 mm). In addition, 8 copper specimens (10 mm diameter, 25 mm height, Cu-OPF: oxygen-free phosphorous doped) and 8 titanium specimens (tube of 6 mm outer and 4 mm inner diameters) were positioned. The specimens were installed on the surface in pre-drilled holes followed by a small bentonite cylinder (Figure 1). The copper specimens were positioned in blocks 16 and 20 at 3 cm distance from the heater in four directions (0°, 90°, 180° and 270°). In the case of titanium specimens, four of them were installed in each of the two chosen blocks (#3 and #15), and inside holes were drilled at mid-height of the block periphery in four directions (0°, 90°, 180° and 270°).

The dismantling operation of the ABM5 experiment began in June 2017. Some blocks looked rather intact, while others were highly fractured and very fragile due to the effect of water loss caused by the high temperature. Different bentonite samples were retrieved and analysed for performing different investigations (e.g., [8,9,17]). Most of the bentonite samples were preserved immediately inside vacuum-sealed aluminium-foil bags for avoiding water loss and oxidation due to their exposure to the air-atmosphere.

## 2.2. Materials

For this study, four slices from bentonite samples collected after dismantling were sent to CIEMAT in June 2019 (Figure 1): MX-80 from block position 1 (3 m depth) [18,19], Ibeco from block position 11 (2 m depth) [20], Rokle from block 14 (1.7 m depth) [21,22], FEBEX from block position 25 (0.6 m depth) [23,24], and Asha 505 from block position 28 (0.3 m depth) [25]. These bentonites correspond to mainly Na- (MX-80 and Asha 505) and Ca-Mg-smectites (Rokle, FEBEX and Ibeco) [18]. As additional main differences: (a) Rokle and Asha 505 bentonites have a high content of secondary iron oxides, (b) Ibeco and MX-80 contain pyrite, and (c) Ibeco contains a higher amount of carbonates (total carbon of 1.2 wt.%) than MX-80 and FEBEX bentonites (0.3 wt.% and 0.1%wt. of total C, respectively).

In the laboratory, the received portion of each ring-shaped bentonite block was sampled along one radius. The samples were sliced in several fragments with a knife from the granite contact towards the heater contact. Several subsamples were used for different analyses (Figure 3).



**Figure 3.** Sampling of the bentonites at laboratory for performing different analyses.

### 2.3. Analytical Methods

The objective of the laboratory tests was to undertake a comprehensive analysis of the blocks in order to determine the physical, physico-chemical, mineralogical and geochemical characteristics of the buffer for the assessment of the properties of the bentonite material after the heating and hydration process over the 4.4 years of the experiment.

#### 2.3.1. Physical Properties

The gravimetric water content, w.c., expressed as a percentage, is defined as the ratio between the weight of water lost after heating the sample at 110 °C for 48 h in an oven and the weight of dry solid.

Dry density,  $\rho_d$ , is defined as the ratio between the weight of the dry sample and its volume occupied prior to drying. The volume of the solid samples was determined by means of the mercury displacement method (UNE Standard 7045).

Total physical porosity or total porosity was calculated by means of the relationship:  $n = \left(1 - \left(\rho_{bulk,dry} / \gamma_s\right)\right) \times 100[\text{vol}\%]$ , where  $\rho_{bulk,dry}$  is the bulk dry density and  $\gamma_s$  is the grain density or specific gravity of the solid sample.

### 2.3.2. Mineralogical Analysis

XRD diffraction patterns were obtained from random powders and oriented aggregates by using a Philips X'Pert –PRO MPD diffractometer, equipped with a fixed divergence slit (0.1245° size), Scientific X'celerator detector and an anticathode Cu-K $\alpha$  at 45 kV and 40 mA. The samples were analysed from 2° to 70° 2 $\theta$  with a step size of 0.017° 2 $\theta$ . The scan rate per step for the powder samples was 50 s. HighScore program v.5 was used for mineral identification and quantitative analyses, with the Power Diffraction File database from the International Center for Diffraction Data (ICDD).

The fine fraction of less than 2  $\mu\text{m}$  was obtained by suspension and sedimentation in deionised water by using the modified Jackson treatment [26,27]. The final clay suspension was ultrasonically dispersed using 1 g in 5 mL of deionized water. Oriented mounts (air dried, ethylene glycol solvated and 550 °C heated) were analysed by using a Bruker D8 Advance diffractometer with an anticathode Cu-K $\alpha$  at 40 kV and 30 mA, equipped with a fixed divergence slit (0.15° size). The samples were investigated from 2° to 35° 2 $\theta$  with a step size of 0.02° 2 $\theta$  and a scan rate of 2 s per step.

Fourier Transform Infrared (FTIR) spectra were obtained in the middle-IR region (4000–400  $\text{cm}^{-1}$ ) by using a Nicolet iS50 with a DTGS KBr detector (resolution 4  $\text{cm}^{-1}$ , 32 scans) on KBr-pressed discs in transmission technique. The atmosphere was continuously purged from water and atmospheric CO<sub>2</sub>. Two milligrams of powdered air-dried sample were dispersed in 200 mg of KBr and pressed into a clear disc.

Scanning electron microscopy (SEM). A JEOL JSM-820 SEM microscope coupled with a X Oxford ISIS Link energy dispersive X-ray energy spectrometer (XEDS). Prior to the analysis, the samples were dried at 40–60 °C in an oven overnight, and then subjected to gold metallization by applying 5  $\times 10^{-2}$  Torr vacuum and a gold coating of 300 to 400 Å thickness, using a BALZERS SCD 004 sputter coater. The composition of dioctahedral smectites and illites was calculated using the structural formula method according to [27,28], on the basis of 11 oxygen atoms equivalent per half unit cell (e.phuc<sup>-1</sup>), tetrahedral occupation by 4.0 cations (<sup>IV</sup>Si + <sup>VI</sup>Al), octahedral occupation by 2 cations, and complete oxygen/hydroxyl framework of O<sub>10</sub>(OH)<sub>2</sub>. For chlorites [ . . . O<sub>10</sub>(OH)<sub>2</sub>-1H<sub>2</sub>O] and kaolin-ites [ . . . O<sub>5</sub>(OH)<sub>4</sub>-1H<sub>2</sub>O], 14 and 7 oxygen atoms e.phuc<sup>-1</sup> were used, respectively.

XPS. X-ray photoelectron spectroscopy (XPS) data were recorded using a Phoibos-150 electron analyser (SPECS) under a pressure lower than 2  $\times 10^{-9}$  mbar using Al K $\alpha$  radiation. The wide scan spectra and the narrow (high resolution) spectra were recorded using a constant pass energy of 100 and 20 eV, respectively. The binding energy (BE) scale was referenced to the BE of the main C-C contribution (284.6 eV) of the C 1s spectrum corresponding to the adventitious contamination layer. All of the spectra were computer-fitted using pseudo-Voigt line profiles and the CASAXPS software. Relative atomic concentrations were calculated by peak integration after background subtraction using the Shirley method and the atomic sensitivity factors tabulated by Wagner [29].

Mössbauer spectroscopy. <sup>57</sup>Fe Mössbauer spectroscopy data were recorded at room temperature (300 K) in transmission mode using a conventional constant acceleration spectrometer and a <sup>57</sup>Co (Rh) source. Absorbers were prepared to have an effective thickness of about 5–10 mg of natural iron per square centimetre. The velocity scale was calibrated using a 6  $\mu\text{m}$ -thick natural iron foil. All the spectra were computer-fitted using Lorentzian lines and the isomer shifts were referred to the centroid of the  $\alpha$ -Fe sextet at room temperature.

### 2.3.3. Geochemical Analysis of Solid Samples

#### *X-ray Fluorescence*

The major elements (SiO<sub>2</sub>, Al<sub>2</sub>O<sub>3</sub>, Fe<sub>2</sub>O<sub>3</sub>, MnO, MgO, CaO, Na<sub>2</sub>O, K<sub>2</sub>O, TiO<sub>2</sub>, P<sub>2</sub>O<sub>5</sub> and SO<sub>3</sub> in %) were analysed by using an Axios X-ray Fluorescence (XRF) spectrometer

from Panalytical equipped with a rhodium X-ray tube (stimulation power: 1 KW). The dissolution or decomposition of the samples into a homogeneous glass was obtained by fusion, which consisted of heating a mixture of the sample (0.8 g) and a flux of 7.2 g of  $\text{Li}_2\text{B}_4\text{O}_7$  at high temperatures (800 to 1000 °C). The end-product after cooling was a one-phase glass. The whole material was melted stepwise in a platinum crucible at a smelting apparatus. After this procedure, the melt was transferred into a platinum jacket and cooled. The loss of ignition was determined separately by oven-drying the dried sample at 1025 °C for 3 h.

#### *Chemical Total Carbon and Total Sulfur*

Total carbon, total sulfur and total inorganic carbon were determined on 0.2 g of powdered solid samples by means of a LECO CS-244 analyser by combustion. The total inorganic carbon (TIC) content was obtained with a TOC- $V_{\text{CSH}}$  analyser (SHIMADZU, Shimadzu Scientific Instruments, Kyoto, Japan) equipped with an SSM-5000A module. The presence of organic carbon was evaluated by the difference between TC and TIC.

#### *Chemical Fe(II)- $Fe_{\text{total}}$ in the Samples*

Fe(III) and Fe(II) were leached from the samples by using a modification of the procedure described in [30] and analysed by the 1,10 phenanthroline spectrophotometric method. To a finely ground sample of 0.1–0.2 g, 1 g of  $\text{NH}_4\text{HF}_2$  and 10 mL of 1:1  $\text{H}_2\text{SO}_4$  were added in 40 mL high-density polyethylene (HDPE) tubes. The tubes were closed and heated to 90 °C for 60 min in a shaking water bath. After this extraction process, the tubes were allowed to cool to room temperature. The contents were transferred to 50–100 mL volumetric flasks and made up to volume with MilliQ water. The phenanthroline method was used for the determination of Fe(II).

### 2.3.4. Physico-Chemical Characterization

#### *Cation Exchange Capacity*

Total CEC was measured with 0.01 M copper triethylenetetramine, Cu-Trien or  $[\text{Cu}(\text{Trien})]^{2+}$ , solution [31]. In this process, 200 mg of an air-dried clay sample was weighed in 60 mL centrifuge tubes. Then, 25 mL of deionized water was added, and the suspension was dispersed by ultrasonic treatment for 5 min. Then, 10 mL of 0.01 M  $[\text{Cu}(\text{Trien})]^{2+}$  was added and allowed to react by end-over-end shaking for 1 h. The suspensions were centrifuged at a constant rotation speed of 11,000 rpm for 30 min. Then, 3 mL of the clear blue solution (filtered through 0.2  $\mu\text{m}$  pore size syringe filter) was filled into 1 cm optical glass cuvettes and the absorbance of the solution was measured at 578 nm wavelength by using a Orion Aquamate 8000 spectrophotometer. The analyses were performed in duplicate, with the standard deviation of the measurement being  $\pm 2$  meq/100 g.

#### *Cation Exchange Population*

Cation exchange population was determined by using Cs as the index displacing cation [32]. Solid air-dried samples were equilibrated at a 1:4 solid to liquid ratio (0.25 kg/L) with 0.5 M  $\text{CsNO}_3$  at pH 8.2 inside a JACOMEX glove box (<1 ppm  $\text{O}_2$ ). After phase separation by centrifugation (11,000 rpm, 30 min., outside the glove box), the supernatant solutions were filtered through 0.2  $\mu\text{m}$  pore size syringe filter (inside the anoxic glove box), and the concentration of the major and trace cations was analysed. Sodium and calcium contents were corrected with respect to soluble salts from pore water.

#### *BET External and Total Surface Area*

Nitrogen adsorption/desorption isotherms were obtained by using a Micromeritics ASAP 2020 V3.02 H sorptometer. Around 0.5 g of the total sample were dried at 90 °C for at least 24 h before the tests. Prior to the nitrogen adsorption, the samples were outgassed by heating at 90 °C for 18 h using a mixture of helium and nitrogen under a residual vacuum between 6 and 10  $\mu\text{mHg}$ . External surface areas, corresponding to both the external faces and the edges of the smectite particles, since in the adsorption of non-polar molecules, the layered structure remains closed, were calculated using the standard N<sub>2</sub>-BET method, using a series of data points over the P/P<sub>0</sub> range of 0.02 to 0.25 on the nitrogen adsorption isotherm [33].

In contrast to nitrogen, which is only adsorbed at the external surface of the stacks of the smectite layers, water molecules can be adsorbed onto the whole surface, including both the internal (interlayer) and external surfaces of the clay minerals. Thus, in order to obtain the total specific surface area (SA), water vapour gravimetric adsorption measurements were performed by Keeling's hygroscopic method [34] by storing the samples at a constant 75% relative humidity atmosphere in a chamber over-saturated in NaCl solution for 1 month. Prior to the tests, the samples were dried at 110 °C for 24 h. The weight changes of the samples as a result of the adsorbed amount of water were measured and related to the total surface area, SA.

#### *Soluble Salts by Aqueous Leaching*

Aqueous extract solutions were used for analysing the soluble salts and ion inventories. The crushed subsamples were placed in contact with deionised and degassed water at a 1:4 solid to liquid ratio, shaken end-over-end and allowed to react for one day under anoxic conditions inside an anoxic glove box. After phase separation by centrifugation (30 min at 11,000 rpm), the supernatant solutions were filtered through a 0.2 µm pore-size syringe filter (inside the anoxic glove box) and analysed. Aqueous leaching conditions were selected to suppress mineral oxidation, by working in an oxygen-free atmosphere, and to avoid large modifications of cation concentration at exchange sites by carbonate dissolution, which affects the cation distribution in the aqueous extract solution. All the tests were performed for one day, since a carbonate equilibrium in bentonites usually requires more than six days (e.g., [24,35]).

#### 2.3.5. Pore Water Chemistry

The pore water of the bentonite samples was obtained by means of the squeezing technique at high pressures [36–38]. Squeezing is analogous to the natural process of consolidation, caused by the deposition of material in geological time, but at a greatly accelerated rate. The squeezing process involves the expulsion of interstitial fluid from the saturated clayey material being compressed [39].

At CIEMAT, the squeezing rig is similar to that developed by [39,40]. The squeezer was designed to allow a one-dimensional compression of the sample by means of an automatic hydraulic ram operating downwards, the squeezed water being expelled from the top and bottom of the cell into a vacuum vial (Figure 4). The compaction chamber is made of type AISI 329 stainless steel (due to its high tensile strength and resistance to corrosion) with an internal diameter of 70 mm. The compaction chamber is 250 mm high with 20 mm wall thickness and allows pressures up to 100 MPa.

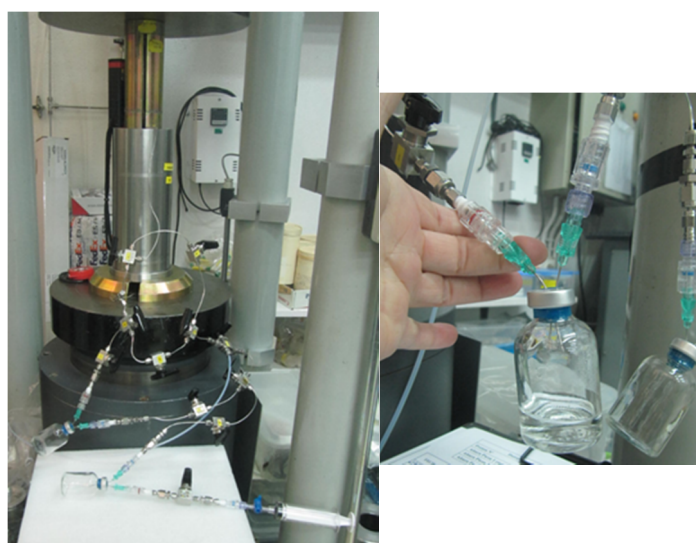


**Figure 4.** Squeezing technique for collecting the pore water from bentonite blocks.

The filtration system allows the extraction of interstitial water by drainage at the top and at the bottom of the sample. This system comprises a 0.5  $\mu\text{m}$  stainless steel AISI 316L porous disk (Cr 17.36%, Ni 11.4%, Mo 2.15%, Si 0.94%, Mn 0.17%, C 0.027%, S 0.011%, P 0.022%, Fe 66.92%) in contact with the sample. The liquid is collected through stainless steel tubes ( $1/16$  inch) in a vacuum vial sealed by a septum. The whole system remains under ambient conditions (room temperature of about 22–25 °C). However, a sampling circuit was designed for collecting the water at anoxic conditions (Figure 4). At the beginning of the test, the squeezing cell and all the sampling tubing and vials were closed to ambient conditions. Then, several Ar-flushing and vacuum cycles were performed, keeping the system under anoxic conditions.

The bentonite samples for squeezing were prepared using a knife to remove the outer part in order to discard possible contaminated material. The sample was cut into a cylindrical shape, weighed and placed into the body of the cell. A small stress of 1 to 5 MPa was initially applied to remove most of the atmospheric gas from the cell and allow the sample to bed in. After applying two additional Ar-flushing and vacuum cycles to the sampling circuit, the stress was progressively increased up to the selected pressure, rather than in a single step. This avoids overconsolidation or collapse of the clay-pore system. When the maximum amount of squeezed water was obtained for a given pressure, the vial was removed, keeping the sample away from any contact with the atmosphere. The water sample collected was weighed and immediately analysed. The bentonite mass was also weighed, and the final water content and dry density were determined. During the squeezing test, the evolution of the pressure, axial strain and changes in the length of the sample due to consolidation were recorded over time by using a data acquisition system. The chemical analysis of the water samples was performed with the methods described in Section 2.3.6.

### 2.3.6. Water Chemical Analyses

The water samples were filtered through 0.2  $\mu\text{m}$  syringe filters, except those for pH and electrical conductivity (EC) measurements. The pH was measured by means of an ORION 720A pH-meter equipped with a Metrohm 6.0224.100 combined pH micro-electrode. The total alkalinity of the water samples was determined by using a Metrohm 888 Titrand equipment (5 mL burette and a 6.0224.100 Metrohm combined pH micro-electrode), with a specific dynamic equivalence point titration (DET) method. The major and trace cations, including silica, were analysed by means of inductively coupled plasma optical emission spectrometry (ICP-OES) in an Agilent 5900 synchronous vertical dual view (SVDV) spectrometer. Sodium and potassium were determined by atomic absorption spectrometry in an Agilent AA 240 FS spectrometer. Anions were analysed by ion chromatography by using a Dionex ICS-2000 equipment.

## 3. Results

### 3.1. Physical Properties

The characteristics of the bentonite blocks at initial conditions before the *in situ* experiment are given in Tables 3 and 4. The initial water content is between 10.6 and 17.2%, the dry density is between 1.80 and 1.93  $\text{g}/\text{cm}^3$  and the degree of saturation is between 67 and 84%. After 4.4 years of artificial hydration and heating, the samples increased their water content up to  $\sim 30 \pm 2\%$ , showing lower values closer to the heater contact. The dry density decreased up to  $\sim 1.52 \pm 0.05 \text{ g}/\text{cm}^3$ , with a tendency to increase closer to the heater contact (Table 4). It is interesting to note that although complete saturation was achieved, the degree of saturation increased from the top to the bottom of the bentonite package (from 93 to 100% of saturation), as described in [8], probably due to gravity, the highest temperatures in the central part, and the steam–bentonite interactions at the top of the bentonite package (Figure 2).

**Table 4.** Physical properties of bentonite blocks analysed (see locations in Figure 3).

Subsample	Distance to Heater (cm)	Water Content w.c. (%)	Grain Density (g/cm <sup>3</sup> ) <sup>1</sup>	Dry Density (g/cm <sup>3</sup> )	Porosity (%)	Degree of Saturation (%)
Asha Block 28 granite (G)	8.33	30.3	2.869	1.49	0.48	93
Asha Block 28 central (M)	5.00	29.9	2.869	1.49	0.48	92
FEBEX Block 25 granite (G)	8.33	28.1	2.735	1.51	0.45	94
FEBEX Block 25 central (M)	5.00	27.8	2.735	1.51	0.45	94
Rokle Block 14 granite (G)	8.33	29.9	2.940	1.63	0.45	109
Rokle Block 14 central (M)	5.00	28.2	2.940	1.58	0.46	96
IBECO Block 11 granite (G)	8.33	33.1	2.753	1.44	0.48	100
IBECO Block 11 heater (H)	1.67	30.9	2.753	1.56	0.43	112
MX-80 Block 1 granite (G)	8.33	32.5	2.735	1.46	0.47	102
MX-80 Block 1 heater (H)	1.67	29.8	2.735	1.52	0.45	101

<sup>1</sup> [5].

### 3.2. Mineralogy

#### 3.2.1. XRD Analysis

The random powder patterns of the samples analysed show the strongest (001) reflection of smectite located at ~14–15 Å indicative of a two-layer hydrate Ca-Mg-Montmorillonite (Figure S1 from Supplementary Data, Figure 5). This is due to the saline Na-Ca-Cl-groundwater/bentonite interactions which provoked cation exchange reactions. Na-bentonites (MX-80 and Asha 505) have changed the character of the smectite particles acquiring a Ca-character, shifting d(001) values from 12 Å to 15 Å. In turn, the initial Ca-bentonites (FEBEX, IBECO, Rokle) reveal two populations of water-hydrated montmorillonite clay particles, increasing the one-layer hydrate Na-montmorillonite component (~12 Å). None of the bentonites showed significant indication of any smectite loss or transformation.

d(006) XRD reflexion was centred at 1.49–150 Å both in reference and retrieved samples, with no changes being observed even in the samples located at the heater contact (Figure 5). This indicates that the presence of neoformed trioctahedral smectites (saponite), appearing at 60–61° 2θ, can be ruled out after the experiment, in contrast to former ABM experiments [5,6,41] or in other *in situ* experiments, such as the FEBEX *in situ* test [42].

XRD analyses of oriented aggregates were performed to verify possible changes in clay mineral particles, increasing Illt/Sme interstratified and/or mixed-layered clay minerals after the high-temperature heating experiment. However, no significant differences are observed in the oriented aggregates (Figure 6, Figure S2 from Supplementary Material). The dioctahedral smectites preserve their expandability (i.e., no illitization), according to the (001) reflexion around 17 Å in the EG XRD pattern for all samples, which indicates complete expansion of the interlayer sites. Kaolinite was present in the reference sample of Asha 505 bentonite, and it is not a neoformed clay mineral.

Regarding other accessory mineral phases (Figure S1 from Supplementary Material and Figure 5), Asha 505 bentonite block 28 showed the highest mineralogical differences in the sample at contact with the heater interface, in which gypsum, Na-clinoptilolite and an increase in calcite and Fe-oxides (goethite, hematite) were observed. FEBEX bentonite block 25 shows an increase in calcite, feldspars and the presence of goethite (Figure S1). Rokle bentonite block 14 increased the amount of goethite, hematite, calcite, dolomite and the presence of siderite. IBECO bentonite block 11 showed similar patterns to the original bentonite sample, except for the absence of calcite. MX-80 bentonite block 1 shows increased amounts of calcite, gypsum, goethite and hematite and the presence of monohydrocalcite, siderite and pyrite.

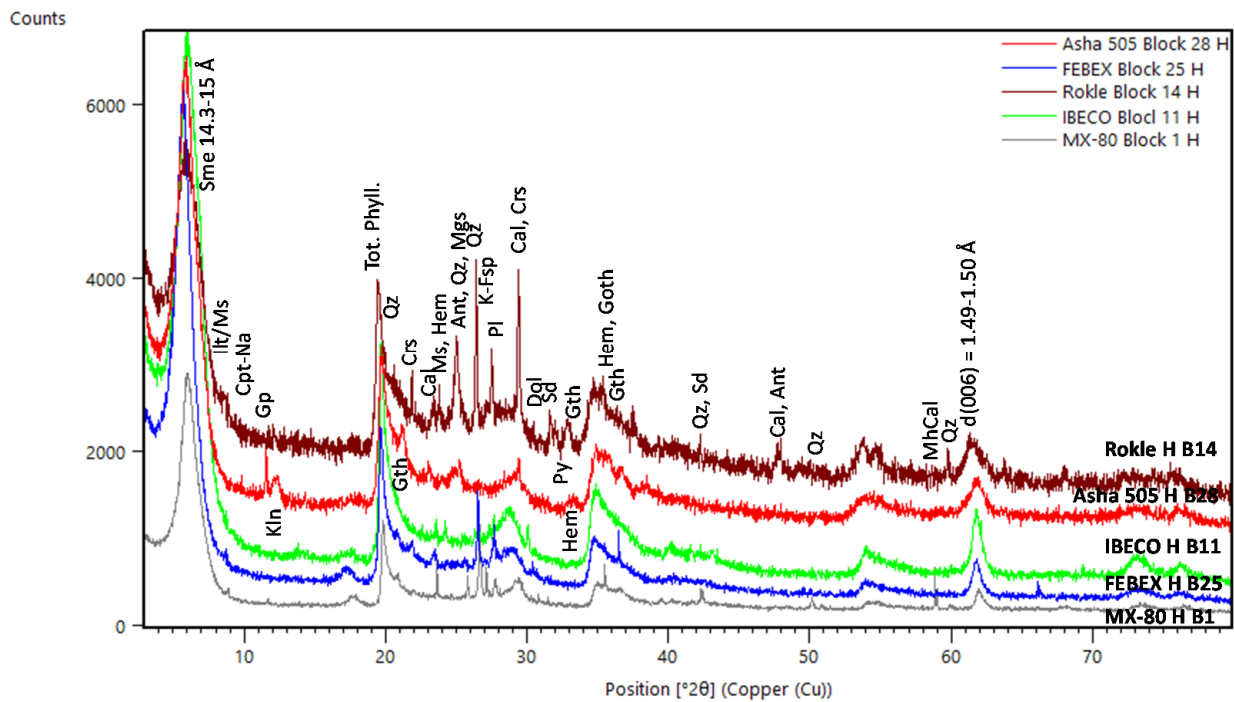


**Figure 5.** XRD patterns of bulk samples from ABM5 experiment. Symbols according to [43]. Sme: smectite, Ilt/Ms: illite/muscovite, Cpt-Na: Clinoptilolite, Gp: Gypsum, Tot. Phyll: total phyllosilicates, Crs: cristobalite, Cal: calcite, MhCal: monohydrocalcite, Qz: quartz, K-Fsp: potassium feldspar, Pl: Plagioclase, Dol: dolomite, Gth: goethite, Hem: hematite.

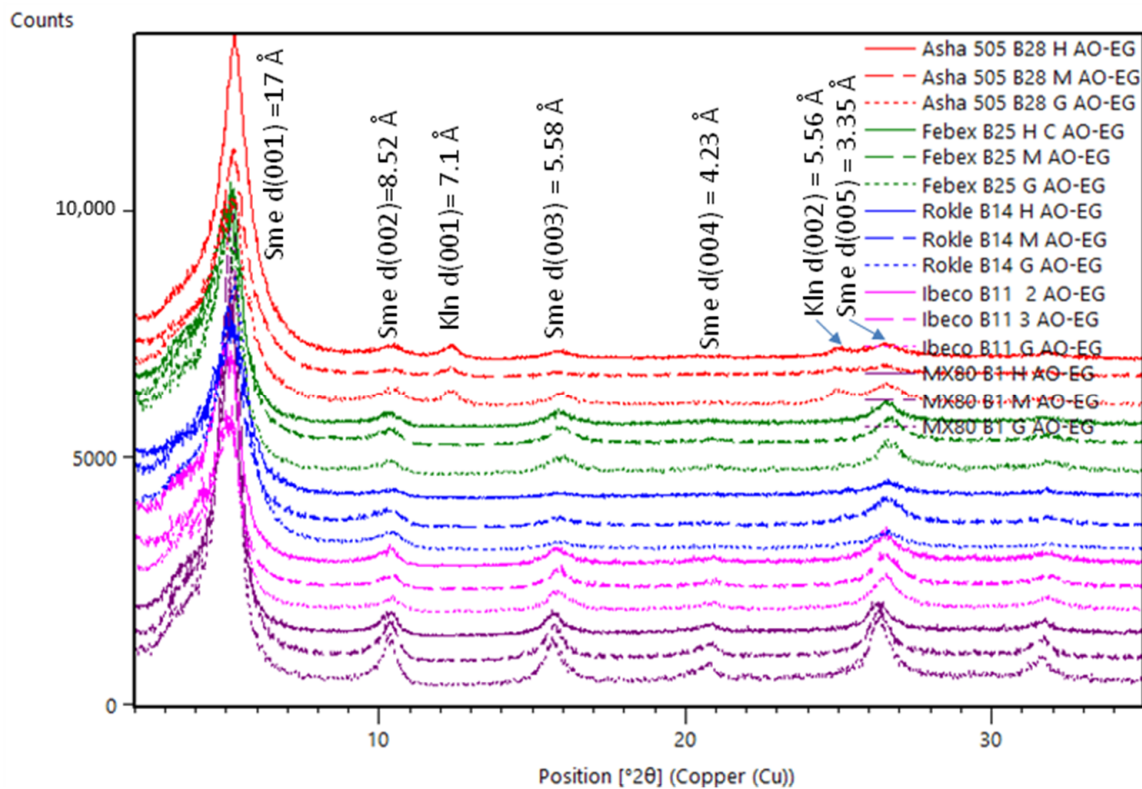


**Figure 6.** XRD patterns of oriented aggregate samples (after ethylene glycol treatment).

### 3.2.2. FTIR Analysis

The bentonite samples were also analysed by FTIR for acquiring information on possible changes in the smectite structure, chemical composition and surface properties due to chemical modifications, as well as to investigate mineral neoformations.

The spectra from the bulk samples of different bentonite blocks are shown in Figures 7 and 8. All spectra include the main typical dioctahedral smectite bands (Table S2 from Supplementary Material). The spectra show a band at  $3627\text{ cm}^{-1}$  which corresponds to the typical OH stretching region of structural hydroxyl groups for dioctahedral smectites with Al-rich octahedral sheets. These are inner hydroxyl groups lying between the tetrahedral and octahedral sheets. The broad band near  $3426\text{ cm}^{-1}$  is due to stretching H-O-H vibrations of adsorbed water, while the band at  $1642\text{ cm}^{-1}$  corresponds to the OH deformation or bending adsorption of water. However, additional bands around  $3697\text{ cm}^{-1}$  indicate the presence of kaolinite in the Asha 505 and Rokle samples, initially present in the raw samples. If the Si-O absorptions and OH bending bands in the  $1300\text{--}400\text{ cm}^{-1}$  range are examined, only one broad, complex Si-O stretching vibration band at around  $1030\text{ cm}^{-1}$  is seen, which is typical of dioctahedral montmorillonite. In this range, the occupancy of the octahedral sheet can be distinguished due to each cation strongly influencing the position of the OH bending bands, which arise from vibrations of the inner and surface OH groups. In all samples, the presence of a peak at  $915\text{ cm}^{-1}$  ( $\delta\text{AlAlOH}$ ) is observed, which is typical of dioctahedral smectites. All samples from bentonites Febex, Ibeco and MX-80 show a band at  $\sim 840\text{ cm}^{-1}$  ( $\delta\text{AlMgOH}$ ), indicating a partial substitution of octahedral Al by Mg. Asha 505, Rokle and MX-80 samples reflect an additional partial substitution of aluminium by iron ( $\delta\text{AlFeOH}$ ), with the band at  $874\text{--}885\text{ cm}^{-1}$ . However, the Fe substitution is much higher in Asha 505 samples due to the decrease in the  $\delta\text{AlMgOH}$  peak and the increase in the  $\delta\text{AlFeOH}$  peak. The adsorption band at  $622\text{ cm}^{-1}$  can be attributed to a R-O-Si vibrations (R = Al, Fe, Mg) in smectites and indicates a perpendicular vibration of the octahedral cations and their connection to the tetrahedral sheet. The bands at  $520\text{ cm}^{-1}$  and  $466\text{ cm}^{-1}$  correspond to Si-O-Al vibration of aluminium in the tetrahedral sheet and Si-O-Si bending vibrations, respectively. All samples show the weak band at  $798\text{ cm}^{-1}$  caused by the Si-O stretching of quartz. Calcite ( $\sim 1426\text{ cm}^{-1}$ ) is observed in Asha 505, Rokle, Ibeco and MX-80 samples. However, this peak disappears in all the analysed retrieved samples from the Ibeco bentonite block 11, as seen in XDR patterns, indicating a high mineral dissolution process in this part of the bentonite package. No other alterations are observed between the initial and retrieved samples from the bentonite blocks analysed.

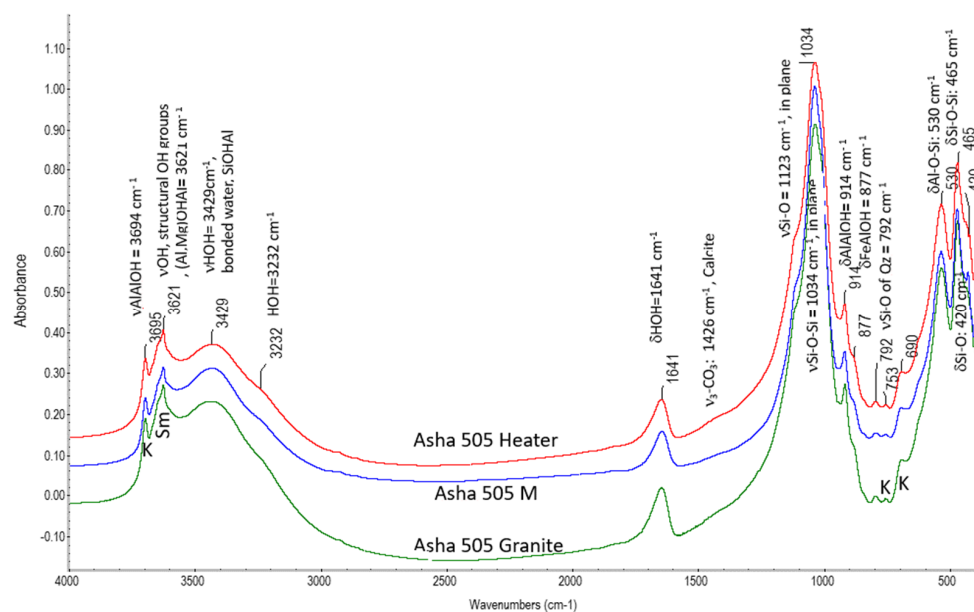


Figure 7. Cont.

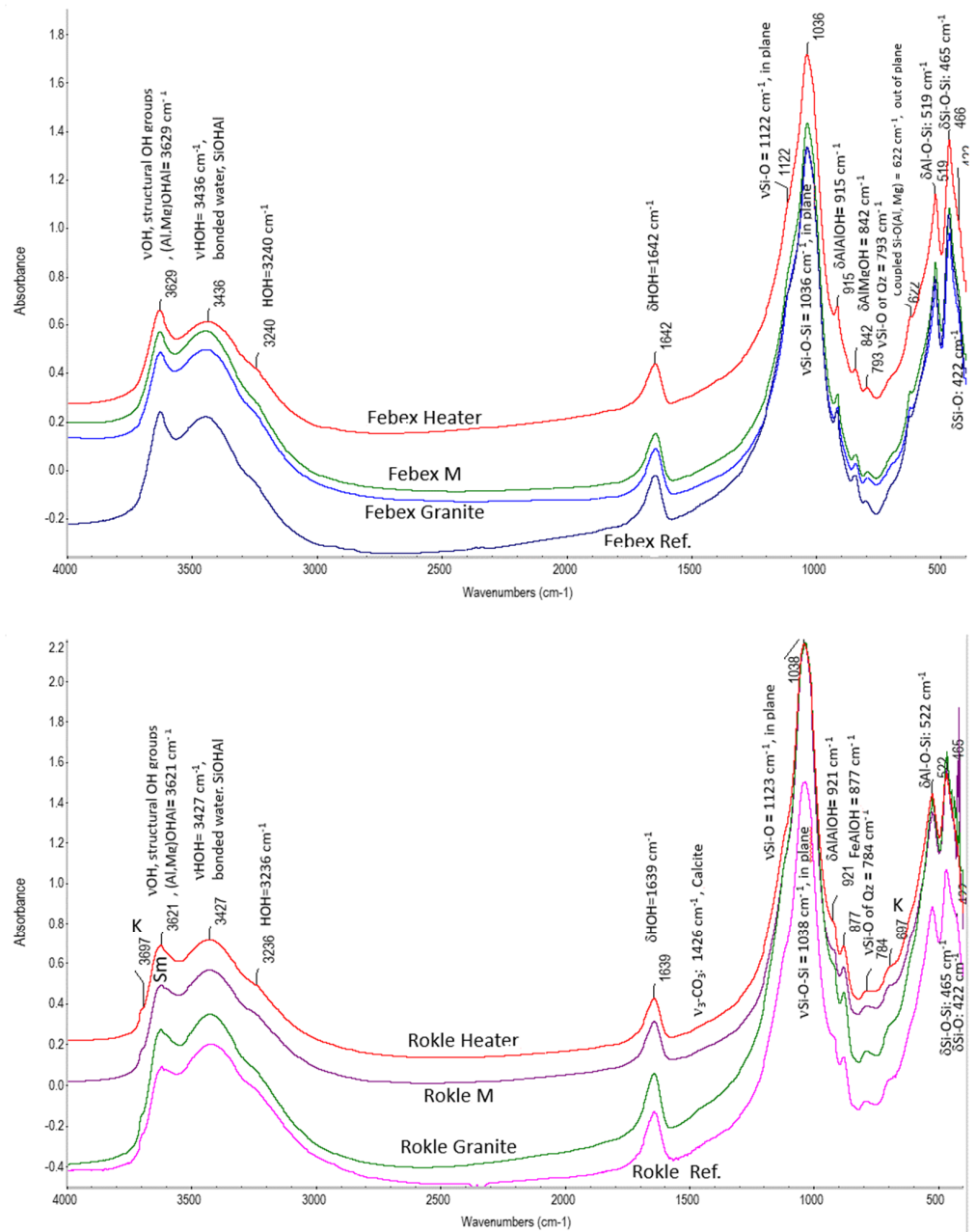
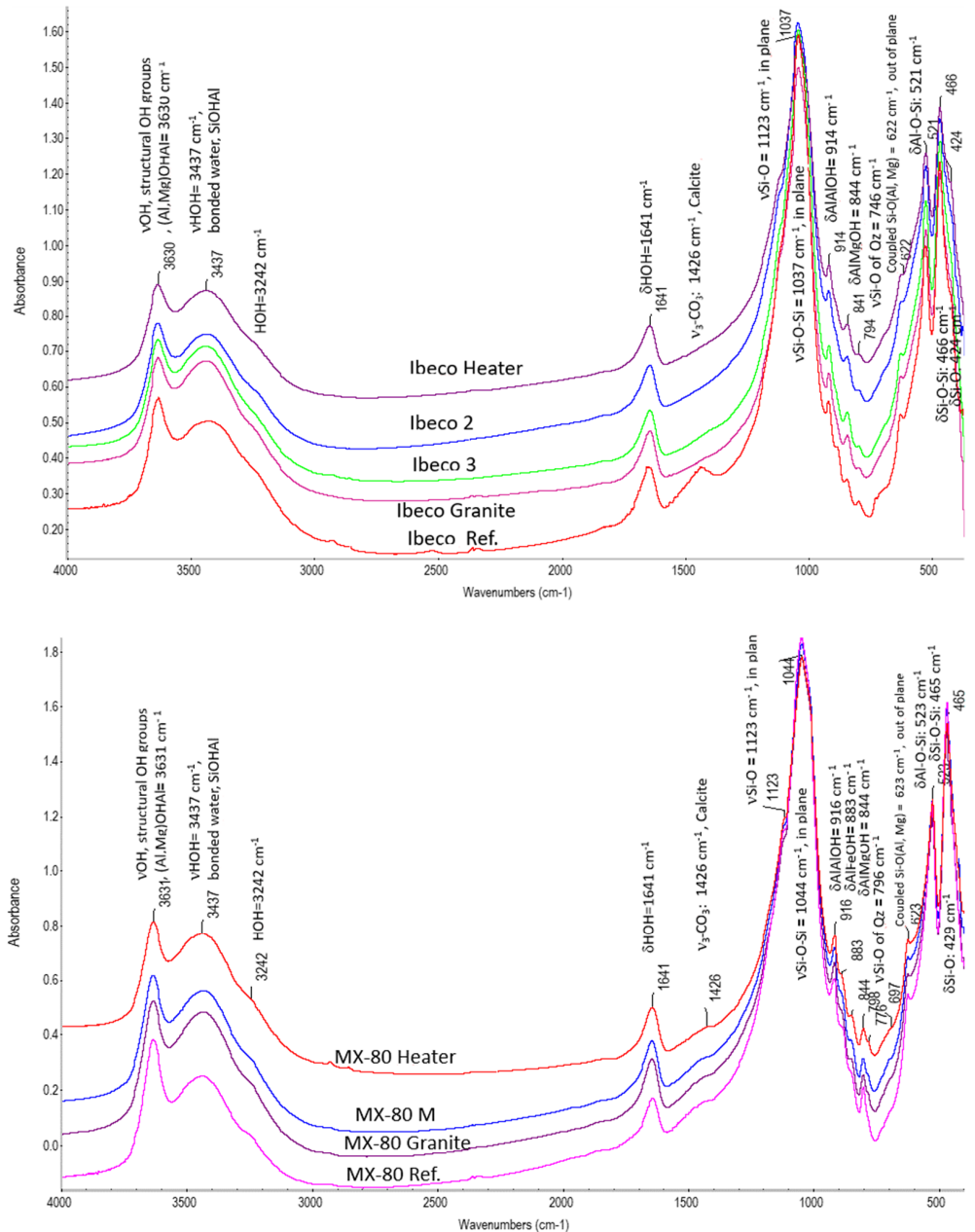


Figure 7. FTIR spectra from samples taken from the ABM5 experiment: Asha 505 block 28 Febex block 25 and Rokle Block 14.



**Figure 8.** FTIR spectra from samples taken from the ABM5 experiment: Ibeco block 11 and MX-80 Block 1.

### 3.2.3. SEM Analysis

Bentonite samples in contact with the heater were analysed by SEM. All of them showed Fe-hydro/oxides indicating the presence of corrosion products near the heater. Barite was found in FEBEX and Rokle samples and pyrite (FeS<sub>2</sub>) and sphalerite (ZnS) in MX-80 samples. All the samples contained organic carbon in some parts (Asha 505, FEBEX, Ibeco). Microorganisms of fungi type (hyphae form) found in FEBEX, Rokle, and Ibeco samples (see OM in Figure 9) may have formed after dismantling during storage due to the high water content of the samples.

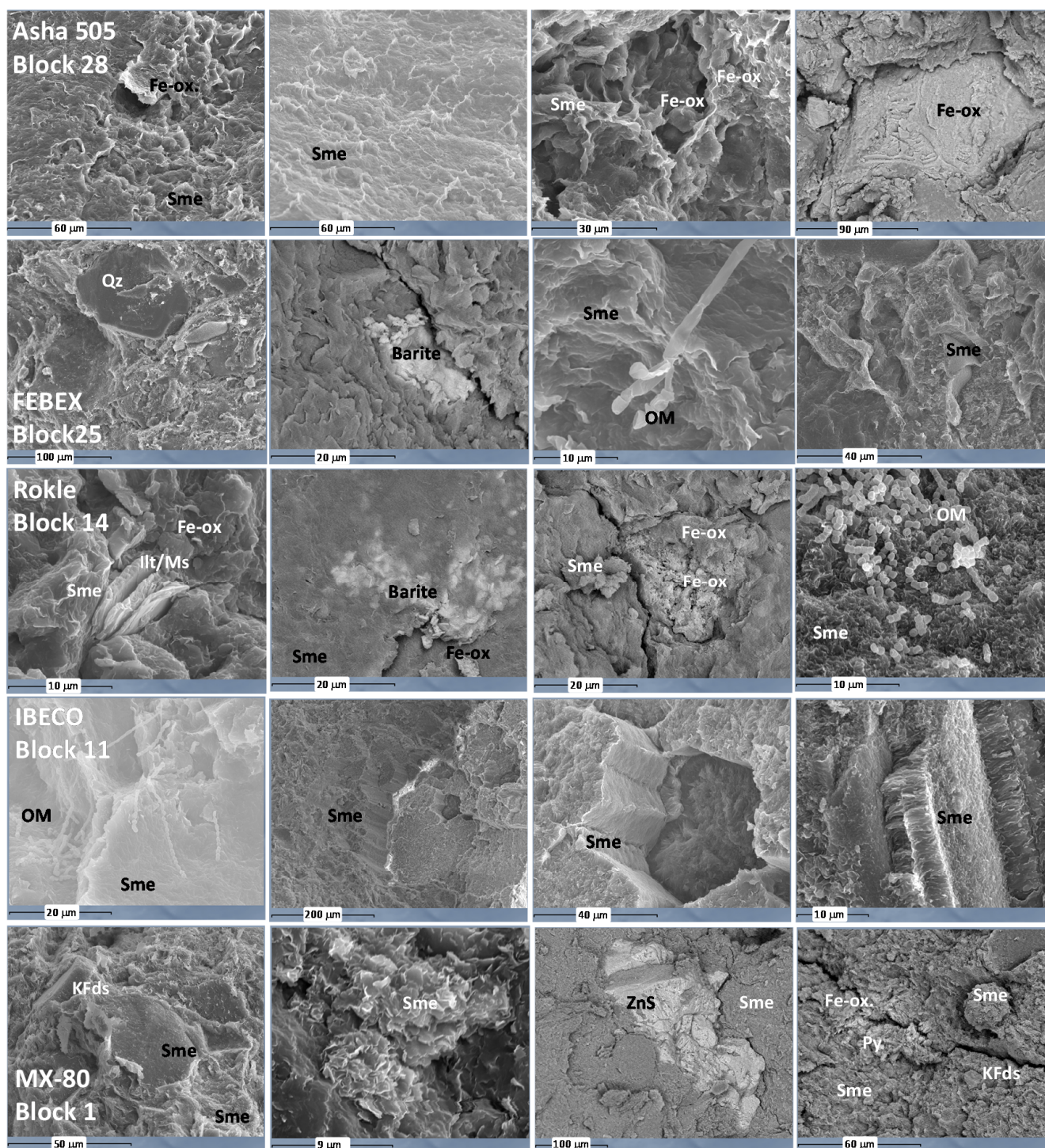


**Figure 9.** SEM photomicrographs from different bentonites in direct contact with the heater (Sme: esmectite, Illt/Ms: illite/muscovite, Qz: quartz, ZnS: sphalerite, Fe-ox: Fe-oxyhydroxides, OM: organic matter (hyphae), Py: pyrite, KFds: potassium feldspars).

The microstructure and composition of the clay mineral particles from samples in contact with the heater were analysed by SEM-EDX. The SEM photomicrographs and the crystallochemical formula of the smectite clay minerals analysed are shown in Figure 9 and Table 5. The structure of the clay mineral particles remains intact, showing a porous honeycomb microstructure, following similar patterns observed in original samples prior to the hydration-heating treatment (see Sme particles in Figure 9). The clay mineral

particles analysed belong to the same chemical composition domain of the smectite clay mineral from the reference samples. However, some particles deviate from the reference crystallochemical structure, the most significant changes being related to changes in the cation composition in tetrahedral sheets, decreasing tetrahedral silicon, increasing tetrahedral charge and total charge of the smectite clay particles. This is true for all samples except for the Rokle bentonite samples, in which the excess of charge is located in tetrahedral sheets originally, and after treatment, there is an increase in the octahedral charge, losing octahedral Al. Fe and Mg content increased in the octahedral sheets, but variations are not significant.

**Table 5.** Structural formula of clay particles analysed in reference samples and close to the heater contact (h.u.c: half unit cell, p.f.u: per full unit cell,  $\tau$  charge: tetrahedral charge, O. charge: octahedral charge).

Sample	Structural Formula	Layer Charge (eq/h.u.c.)	$\Sigma_{tet}$	$\Sigma_{oct}$	$\tau$ Charge (%)	O. Charge (%)	Weight (g/mol) p.f.u.
Asha 505 Ref.	$(Si_{3.81}Al_{0.19})^{IV}(Al_{1.28}Fe^{3+}_{0.48}Mg_{0.24})^{VI}O_{10}(OH)_2(Ca_{0.12}Na_{0.21})_{0.32}$	0.43	4.0	2.00	44	56	764.87
Asha 505 Block 28	$(Si_{3.81}Al_{0.19})^{IV}(Al_{1.10}Fe^{3+}_{0.74}Mg_{0.16}Ti^{4+}_{0.01})^{VI}O_{10}(OH)_2(Ca_{0.12}Na_{0.05}K_{0.05})_{0.33}$	0.33	4.0	2.01	59	41	778.21
	$(Si_{3.84}Al_{0.16})^{IV}(Al_{1.43}Fe^{3+}_{0.32}Mg_{0.23})^{VI}O_{10}(OH)_2(Ca_{0.17}Na_{0.10}K_{0.02})_{0.29}$	0.46	4.0	1.98	36	64	756.05
	$(Si_{3.78}Al_{0.22})^{IV}(Al_{1.17}Fe^{3+}_{0.60}Mg_{0.19}Ti^{4+}_{0.01})^{VI}O_{10}(OH)_2(Ca_{0.17}Na_{0.10}K_{0.02})_{0.29}$	0.48	4.0	1.97	46	54	772.63
	$(Si_{3.62}Al_{0.68})^{IV}(Al_{0.81}Fe^{3+}_{0.98}Mg_{0.24}Ti^{4+}_{0.004})^{VI}O_{10}(OH)_2(Ca_{0.22}Na_{0.05}K_{0.03})_{0.29}$	0.51	4.0	2.04	75	25	798.99
	$(Si_{3.83}Al_{0.17})^{IV}(Al_{1.38}Fe^{3+}_{0.35}Mg_{0.27}Ti^{4+}_{0.03})^{VI}O_{10}(OH)_2(Ca_{0.13}Na_{0.08}K_{0.001})_{0.21}$	0.34	4.0	2.02	50	50	755.41
FEBEX Ref.	$(Si_{3.96}Al_{0.04})^{IV}(Al_{1.49}Fe^{3+}_{0.13}Mg_{0.38})^{VI}O_{10}(OH)_2(Mg_{0.10}Na_{0.20}K_{0.03})_{0.32}$	0.42	4.0	2.00	10	90	742.12
FEBEX Block 25	$(Si_{3.96}Al_{0.04})^{IV}(Al_{1.44}Fe^{3+}_{0.12}Mg_{0.43}Ti^{4+}_{0.01})^{VI}O_{10}(OH)_2(Ca_{0.15}Na_{0.13}K_{0.05})_{0.32}$	0.47	4.0	2.00	9	91	746.71
	$(Si_{3.72}Al_{0.28})^{IV}(Al_{1.32}Fe^{3+}_{0.39}Mg_{0.26}Ti^{4+}_{0.05})^{VI}O_{10}(OH)_2(Ca_{0.15}Na_{0.11}K_{0.03})_{0.29}$	0.44	4.0	2.02	63	37	763.51
Rokle Ref.	$(Si_{3.75}Al_{0.25})^{IV}(Al_{1.19}Fe^{3+}_{0.67}Mg_{0.15}Ti^{4+}_{0.02}Mn^{2+}_{0.01})^{VI}O_{10}(OH)_2(Ca_{0.03}Na_{0.14}K_{0.07})_{0.24}$	0.27	4.0	2.04	93	7	776.00
Rokle Block 14	$(Si_{3.89}Al_{0.11})^{IV}(Al_{0.98}Fe^{3+}_{0.65}Mg_{0.15}Ti^{4+}_{0.08})^{VI}O_{10}(OH)_2(Ca_{0.14}Na_{0.04}K_{0.08})_{0.26}$	0.40	4.0	1.96	27	73	777.36
	$(Si_{3.90}Al_{0.10})^{IV}(Al_{0.98}Fe^{3+}_{0.60}Mg_{0.34}Ti^{4+}_{0.06})^{VI}O_{10}(OH)_2(Ca_{0.17}Na_{0.03}K_{0.10})_{0.30}$	0.47	4.0	1.97	21	79	776.70
IBECO Ref.	$(Si_{3.96}Al_{0.04})^{IV}(Al_{1.48}Fe^{3+}_{0.20}Mg_{0.37}Ti^{4+}_{0.01})^{VI}O_{10}(OH)_2(Ca_{0.04}Na_{0.09}K_{0.02})_{0.15}$	0.20	4.0	2.07	18	82	743.37
IBECO Block 11	$(Si_{4.0})^{IV}(Al_{1.44}Fe^{3+}_{0.12}Mg_{0.39}Ti^{4+}_{0.04})^{VI}O_{10}(OH)_2(Ca_{0.08}Na_{0.18}K_{0.05})_{0.32}$	0.40	4.0	1.99	1	99	745.27
MX-80 Ref.	$(Si_{4.00})^{IV}(Al_{1.51}Fe^{3+}_{0.22}Ti_{0.01}Mg_{0.24})^{VI}O_{10}(OH)_2(Ca_{0.06}Na_{0.15}K_{0.01})$	0.29	4.00	1.98	0	100	744.34
MX-80 Block 1	$(Si_{3.77}Al_{0.23})^{IV}(Al_{1.20}Fe^{3+}_{0.60}Mg_{0.17}Ti^{4+}_{0.02})^{VI}O_{10}(OH)_2(Ca_{0.18}Na_{0.04}K_{0.03})_{0.26}$	0.44	4.0	1.98	53	47	772.58
	$(Si_{3.92}Al_{0.08})^{IV}(Al_{1.65}Fe^{3+}_{0.14}Mg_{0.26})^{VI}O_{10}(OH)_2(Ca_{0.05}Na_{0.06}K_{0.01})_{0.12}$	0.17	4.0	2.06	48	52	738.05

### 3.2.4. XPS and Mössbauer Analysis

For analysing the Fe distribution and speciation inside the bentonite block after the *in situ* test, Rokle bentonite was selected due to its high Fe content. Figure S3 from the Supplementary Material shows the wide scan XPS spectra recorded

from a representative Rokle retrieved sample. The rest of the samples gave very similar spectra. Table 6 collects the atomic percentages obtained from the quantification of such spectra. The atomic concentrations show only minute variations from sample to sample which are within the error of the experimental determination. We must recall that XPS is a surface sensitive technique and, therefore, the quantitative analysis refers to the composition within the characteristic XPS depth probe, which is around 3–5 nm.

**Table 6.** Surface atomic concentrations calculated from the wide scan XPS spectra (in wt.%).

Sample	Fe	O	Ti	Ca	Mg	C	Si	Al
Reference	3.3	52.2	0.7	1.5	3.3	15.4	20.5	3.1
6G	4.4	56.6	0.8	1.3	2.9	11.5	19.5	3.0
5M	4.0	54.7	0.5	1.3	3.2	14.5	15.8	6.0
4H	3.3	53.7	0.9	1.3	3.2	14.8	18.7	4.0

In order to gain insight on the surface chemical states of iron and oxygen, high-resolution spectra were recorded in the Fe 2p and O 1s spectral regions. The spectra were computer-fitted using previous models [44] and the results are presented in Figure 10. The Fe 2p spectra are all very similar. They are composed of an intense main spin orbit doublet (BE Fe 2p<sub>3/2</sub> = 712.3 eV; BE Fe 2p<sub>1/2</sub> = 726.5 eV) and secondary structure: two small shake-up satellites at 722.3 eV and 735.5 eV and a multiplet splitting component at 717.6 eV. These binding energies values and spectral features are all compatible with the presence of Fe<sup>3+</sup>. It is difficult, based on these spectra, to ascertain if there is any small Fe<sup>2+</sup> contribution. As it can be observed in Figure S4 of the Supplementary Information, it is very complicated to separate, in an XPS spectrum, small concentrations of Fe<sup>2+</sup> from the majority presence of Fe<sup>3+</sup> and vice versa.

The O 1s spectra showed in all the cases four different contributions located at 529.7 eV, 531.5 eV, 532.7 eV and 534.7 eV, which correspond to metal-O bonds, Al-O bonds, Si-O bonds and organic carbon/adsorbed water, respectively [45–48]. The spectra show only small differences, except for the increase in intensity of the contribution at 532.7 eV over the course of the series. Although this component is mainly due to Si-O bonds, other contributions due to oxygen-containing functional organic groups or chemi-/physi-sorbed water cannot be discarded either.

Although XPS is a useful technique to determine oxidation states, it lacks the specificity of other techniques, such as Mössbauer spectroscopy, to characterize iron compounds. Hence, <sup>57</sup>Fe Mössbauer spectroscopy was employed to study the speciation of the Rokle samples. Figure 11 shows the room temperature Mössbauer spectra recorded from these materials.

All the Mössbauer spectra were fitted using six different components whose relative areas varied from sample to sample. Whilst the reference samples, 6G (at granite contact) and 5M (at middle bentonite block), gave spectra showing the same contributions in different proportions, the sample 4H close to the heater contact gave a quite different spectrum, showing an additional contribution which was not present in the spectra of the other three. Table 7 collects the hyperfine parameters of the different spectral components and Table 8 shows the relative areas of the components obtained from the fit of the spectra.

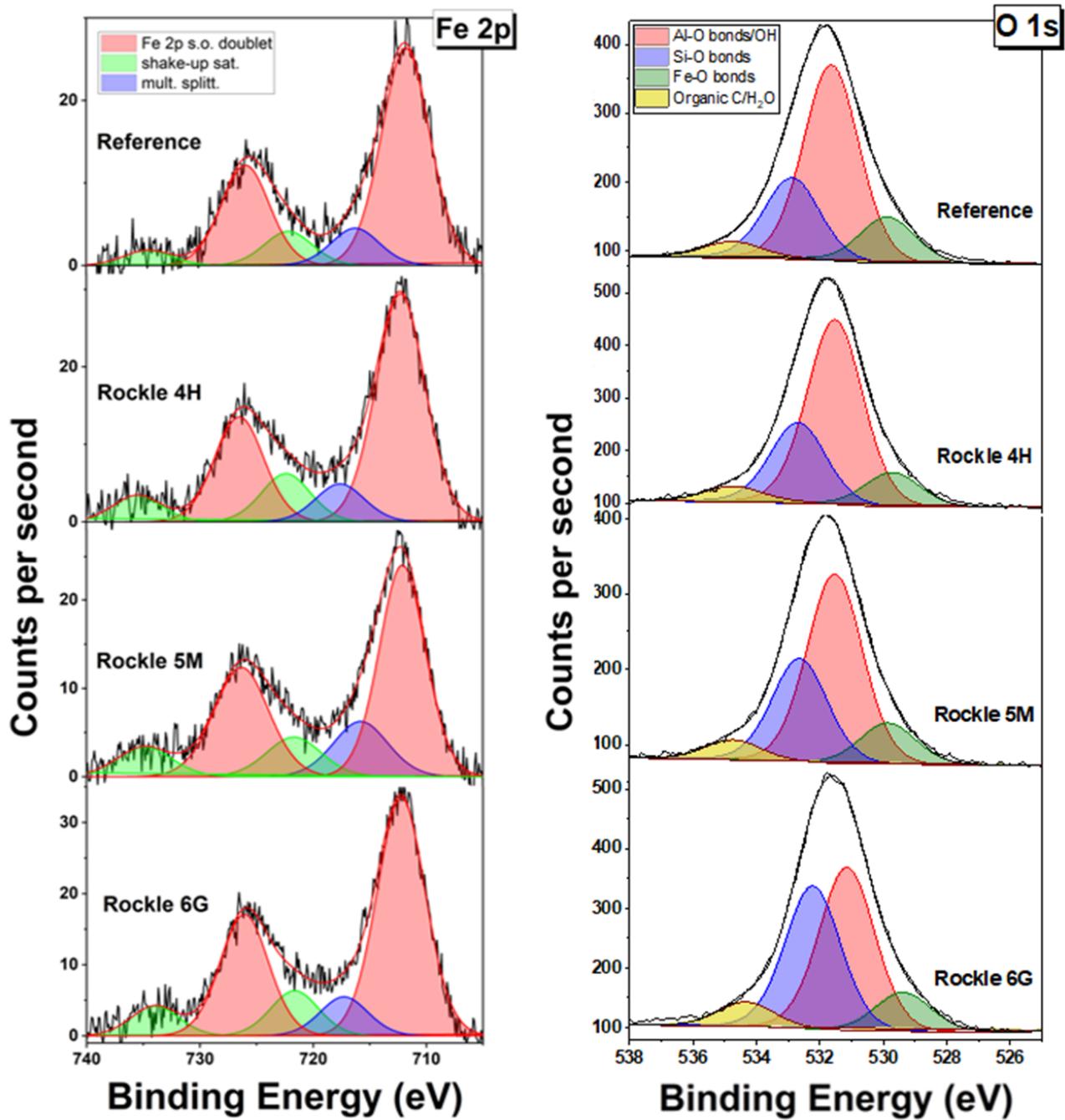


**Figure 10.** XPS narrow scan Fe 2p and O 1s spectra recorded from the Rokle samples: reference, 4H: close to heater interface, 5M: middle, and 6G: close to granite interface; i.e., at 1.67 cm, 5.00 cm and 8.33 cm from the heater contact, respectively.

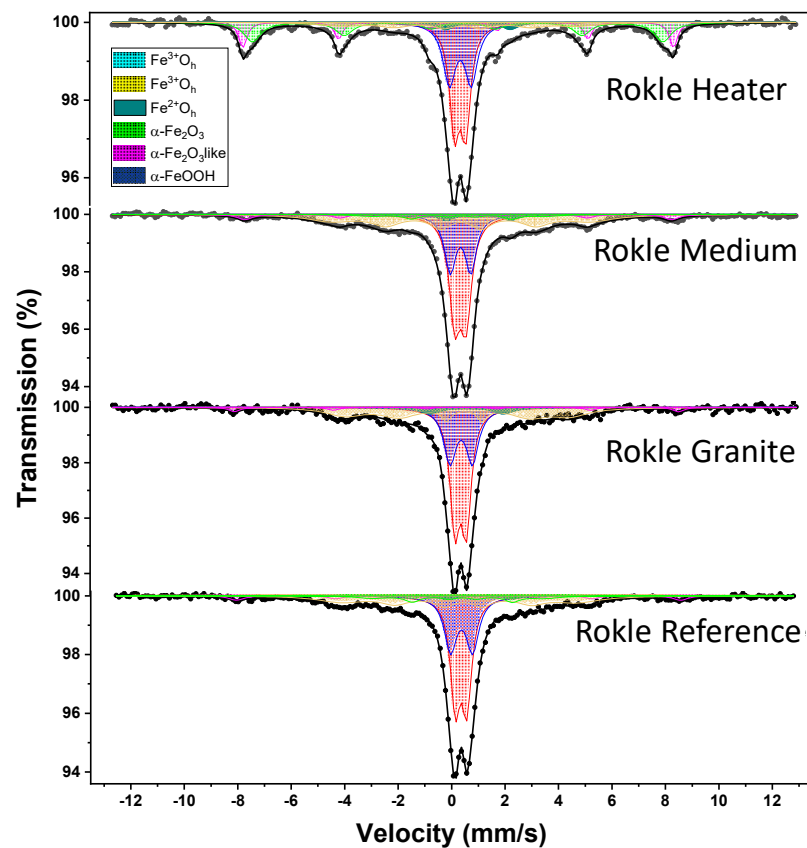


**Figure 11.** Room temperature  $^{57}\text{Fe}$  Mössbauer spectra recorded from the Rokle samples: reference, 4H: close to heater interface, 5M: middle, and 6G: close to granite interface; i.e., at 1.67 cm, 5.00 cm and 8.33 cm from the heater contact, respectively.

**Table 7.** Hyperfine parameters obtained from the fit of the spectra presented in Figure 12.

Hyperfine Parameter	D1	D2	D3	S1	S2	S3	S4
$\delta$ ( $\text{mms}^{-1}$ )	0.36	0.38	1.03	0.37	0.33	0.35	0.37
$\Delta/2\epsilon$ ( $\text{mms}^{-1}$ )	0.44	0.81	2.41	−0.15	−0.14	−0.20	−0.20
H (T)				27.4	20.1	51.0	47.6

$\delta$ , isomer shift;  $\Delta$ , quadrupole splitting, applies to doublets;  $2\epsilon$ , quadrupole shift, applies to sextets; H, hyperfine magnetic field.

**Table 8.** Relative areas obtained from the fit of the spectra presented in Figure 12.

Area (%)	Distance to Heater (cm)	D1 $\text{Fe}^{3+} \text{O}_h$	D2 $\text{Fe}^{3+} \text{O}_h$	D3 $\text{Fe}^{2+}$	S1 $\alpha\text{-FeOOH}$	S2 $\alpha\text{-FeOOH}$	S3 $\alpha\text{-Fe}_2\text{O}_3$	S4 $\alpha\text{-Fe}_2\text{O}_3$ like
Reference		41	29	3	16	7	5	
6G	8.33	37	24	2	25	7	5	
5M	5.00	37	21	3	29	5	5	
4H	1.67	30	23	4	20		12	21

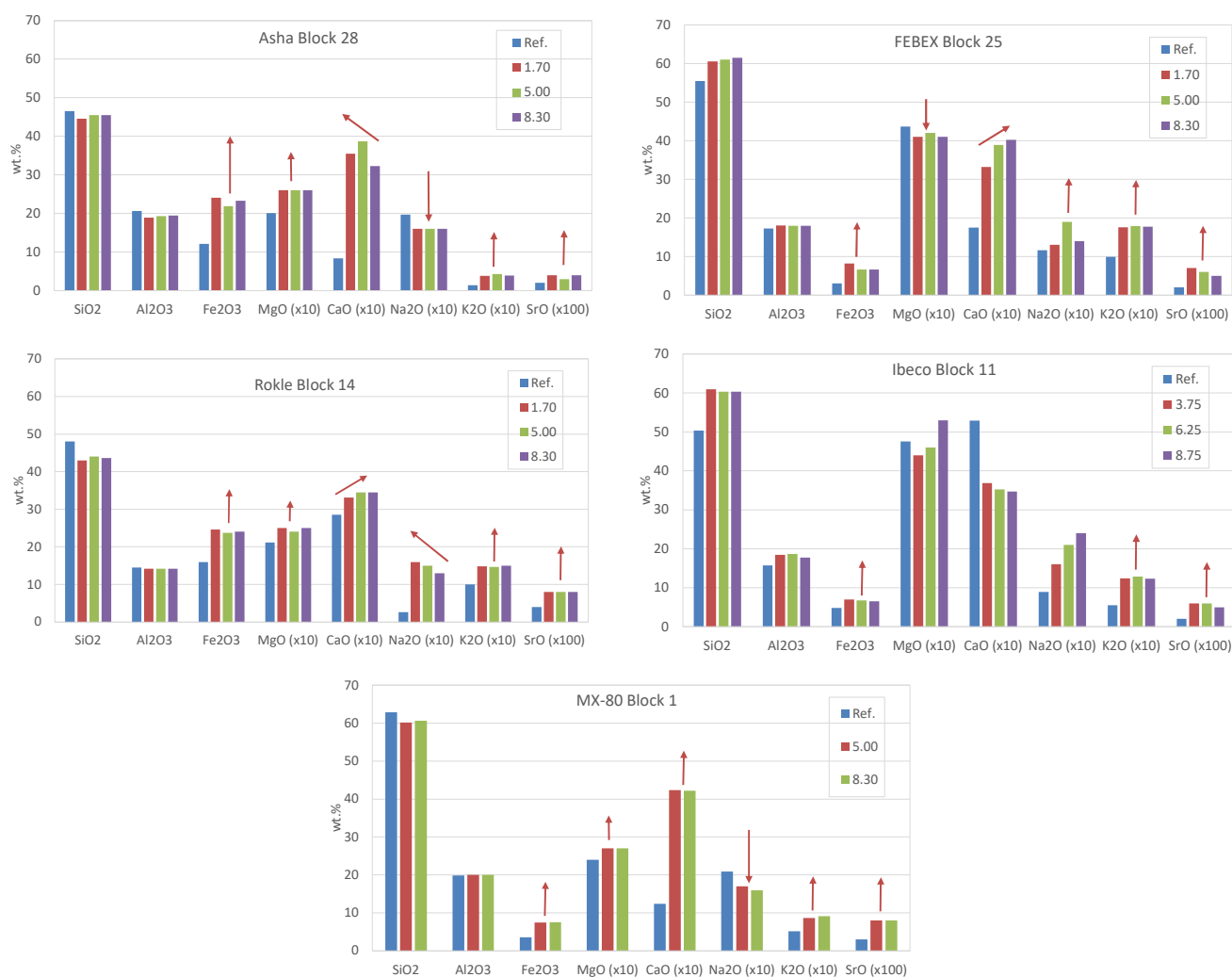


**Figure 12.** Chemical composition of the solid phase (total fraction) prior to and after the dismantling of the ABM5 experiment as a function of the heater distance (1.70 (H), 5.00 (M) and 8.30 (G) cm). Arrows: variations of content (↑: increases or ↓: decreases).

The spectra of the four samples were dominated by an intense central paramagnetic component which was best-fitted to two different quadrupole doublets (D1 and D2). The hyperfine parameters of these doublets (Table 7) are characteristic of high spin  $\text{Fe}^{3+}$  in octahedral oxygen coordination [49]. Since for a high spin  $\text{Fe}^{3+}$  ion (having a half filled  $3d^5$  spherically symmetric configuration) the electric field gradient depends only on the lattice charge distribution, a larger quadrupole splitting,  $\Delta$ , implies a larger distortion from the perfectly symmetrical octahedral coordination [50]. Thus, D1 corresponds to a situation where the  $\text{Fe}^{3+}$  is in a lesser distorted octahedral configuration than that represented by doublet D2. These types of quadrupole doublets are very common in the Mössbauer spectra of bentonites. Sometimes they have been interpreted in terms of cis and trans configurations, associated with the lower and higher  $\Delta$ , respectively [51–53], although some other interpretations consider only that the different  $\Delta$  values result from different geometrical distortions of the coordination polyhedra and/or the existence of different ligands beyond the first coordination shell [54–56]. The highest paramagnetic contribution corresponds to the reference sample while the smallest occurs in the 4H sample (close to heater contact).

Apart from these two  $\text{Fe}^{3+}$  doublets, all the spectra contain a tiny  $\text{Fe}^{2+}$  doublet, accounting for 3–4% of the total spectral area. Because of its small intensity and the many overlapping components, its Mössbauer parameters were best determined by recording

spectra in a lower range of velocities (Figure S4 from Supplementary Material). As shown in Table 7, these Mössbauer parameters (D3) are compatible with an octahedral high spin  $\text{Fe}^{2+}$  species [49]. The spectra recorded from the reference samples 6G and 5M contain a broad magnetic component which was fitted to two broad sextets, S1 and S2. The Mössbauer parameters of these sextets are compatible with microcrystalline goethite [57]. The occurrence of two different goethite sextets might be due to goethite fractions having different particle size or Al substitution. These goethite contributions increase in the order reference  $< 6G < 5M$ . The spectra also show a low intensity (around 5%) magnetic sextet, S3, with parameters typical of hematite [57,58].

As mentioned above, however, the spectrum recorded from the sample 4H located close to the heater contact is quite different. Although the nature of the central paramagnetic region appears to be the same as in the rest of the samples, it contains a much more intense and defined magnetic component characterized by larger hyperfine magnetic fields. This component was fitted to two different sextets, S3 and S4. Sextet S3 is typical of hematite and S4 probably corresponds to a defective hematite phase (“hematite-like phase”) [59]. This sample still contains a noticeable goethite concentration. It is well-known that the dehydration of goethite may result in the formation of hematite [60,61]. Therefore, it seems plausible that this sample, which has been collected close to the heater, contains hematite as a consequence of the loss of OH groups in goethite brought about by the local heating. In addition, these species, or at least a fraction of them, may result from a high-temperature corrosion process occurring at the C-steel heater surface. This sample also contains  $\text{Fe}^{2+}$ . In fact, it is in this sample that it can be observed more clearly due to the lower concentration of goethite whose spectrum overlaps strongly with the  $\text{Fe}^{2+}$  doublet. This result indicates that heating does not affect the  $\text{Fe}^{2+}$  species, probably because it is comfortably sited within the clay mineral structure and is thus difficult to oxidize or cause a slight increase in  $\text{Fe}^{2+}$  within the smectite structure. The presence of magnetite is discarded in all samples analysed.

### 3.3. Geochemistry of the Solid Samples

The geochemical analysis of the main elements in the total fraction of the bentonite material was performed by means of: (a) XRF, (b) combustion (total carbon and sulfur content), and (c) Fe(II)/Fe(III) speciation analysed via  $\text{NH}_4\text{HF}_2\text{-H}_2\text{SO}_4$  leaching tests.

The main changes observed in all the samples are related to iron content, which increased in all samples with respect their reference values (Figure 12 and Tables S3–S4 from Supplementary Material), although other variations are observed. In all of the Ca/Mg-bentonites (Febex and Ibeco), the calcium content slightly decreased, increasing sodium, potassium and strontium contents. However, in all of the Na-bentonites (Asha 505 and MX-80), sodium content decreased, increasing calcium, potassium and strontium content. This seems to indicate a tendency to equilibrate the composition at interlayer sites in all type of bentonites, with a predominance of bivalent cations (see Section 3.4). In addition, those bentonites with an initial higher iron content (Asha 505, Rokle and MX-80) are able to acquire more iron in their structure than those having an initial lower iron content (Figure 12). On the other hand, although the amount of Fe(II) is low with respect to total Fe, Fe(II) content increased in samples close to the heater (Figure 13, Table S5 from Supplementary Material). Variations in the Mg content at exchange sites are less significant in comparison to sodium and calcium, but there is a tendency to increase in the samples with a higher initial Fe content.

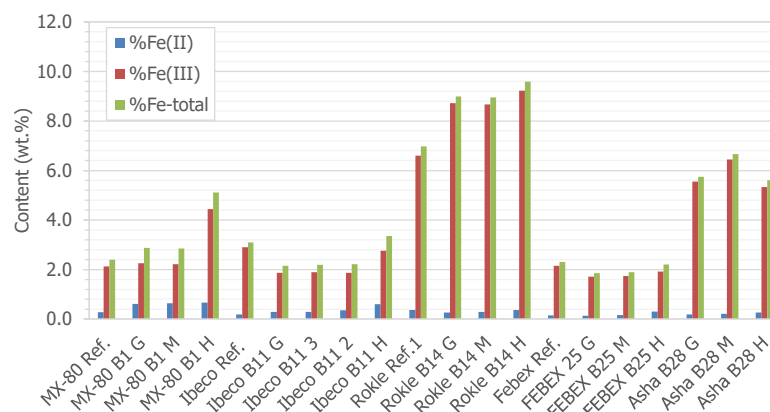


**Figure 13.** Iron content in the solid samples prior to and after the dismantling of the ABM5 experiment: Fe(II), Fe(III) and total Fe.

Regarding carbon and sulfur contents (Table 9), no significant differences are observed, except for the presence of organic matter in the MX-80 bentonite block 1, but the values are lower than in the reference value.

**Table 9.** Total carbon, total sulfur, total surface area (SA) and BET surface area obtained after the dismantling of ABM5.

Sample	Distance to Heater (cm)	Water Content (%) <sup>1</sup>	C <sub>Total</sub> (wt.%)	C <sub>Inorg.</sub> (wt.%)	C <sub>Org.</sub> (wt.%)	S <sub>Total</sub> (wt.%)	Total SA (m <sup>2</sup> /g)	S <sub>BET</sub> (m <sup>2</sup> /g)	CEC (meq/100 g)
Asha 505 Ref. <sup>2</sup>		13.1	0.03	0.02	0.01	0.02			88.6
Asha B28 G	8.3	16.8	0.10	<0.1	<0.1	<0.1	585	65.41	85.8
Asha B28 M	5.0	17.6	0.16	<0.1	<0.1	<0.1	574	55.99	83.9
Asha B28 H	1.7	13.4	0.19	<0.1	<0.1	<0.1	584	61.49	81.3
FEBEX Ref.		14.3	0.12	0.08	0.04	<0.05	628 ± 4	59.2 ± 5	98.1
Febex B25 G	8.3	13.8	0.08	<0.1	<0.1	<0.1	640	38.01	97.6
Febex B25 M	5.0	13.3	0.09	<0.1	<0.1	<0.1	627	45.76	96.5
Febex B25 H	1.7	13.2	0.05	<0.1	<0.1	<0.1	622	36.20	93.1
Rokle Ref.		17.2	0.27	0.10	0.17	0.02	573 ± 5	82.8 ± 0.3	73.8
Rokle B14 G	8.3	8.6	0.26	<0.1	<0.1	<0.1	538	66.90	73.1
Rokle B14 M	5.0	8.9	0.22	<0.1	<0.1	<0.1	549	64.09	73.0
Rokle B14 H	1.7	8.1	0.21	<0.1	<0.1	<0.1	517	58.70	70.3
Ibeco Ref.		14.7	0.79	0.62	0.17	0.23	611 ± 2	57.4 ± 0.4	90.2
Ibeco B11 G	8.75	13.1	0.13	<0.1	<0.1	<0.1	706	49.75	97.1
Ibeco B11 3	6.25	13.1	0.13	<0.1	<0.1	<0.1	688	48.98	97.9
Ibeco B11 2	3.75	13.6	0.15	<0.1	<0.1	<0.1	660	45.04	88.6
Ibeco B11 H	1.25	13.6	0.10	<0.1	<0.1	<0.1	680	51.71	95.0
MX-80 Ref.		10.6	0.28	0.08	0.20	0.24	481 ± 1	29.7 ± 0.2	83.6
MX 80 B1 G	8.3	11.6	0.27	0.16	0.11	0.16	523	21.72	84.1
MX 80 B1 M	5.0	11.6	0.29	0.22	0.07	0.22	542	18.91	87.6
MX 80 B1 H	1.7	11.4	0.24	0.22	0.02	0.22	528	22.48	87.8

<sup>1</sup> from air-dried samples; <sup>2</sup> [5]; G: granite contact; H: heater contact.

### 3.4. Physico-Chemical Properties

The main physico-chemical properties analysed were external (BET) and total surface (SA) areas, total cation exchange capacity (CEC), cation exchange population and the distribution of soluble ions in aqueous extracts.

Total surface area is an important parameter related to the water absorption and swelling capacity of bentonites. It determines the amount of water needed for hydrating all of the clay particles. The lower the particle size, the higher the total surface area. The external surface area of the stacks of layers was determined by N<sub>2</sub>-BET measurements. External BET and total surface area values are given in Table 9. No significant changes are observed in total SA, but a decrease in the external BET surface area is observed

in all of the retrieved samples, with the values being much lower at the heater contact (Figure S5 and Table S6 from the Supplementary Material).

The N<sub>2</sub> adsorption-desorption curves of the samples (reference and retrieved) are shown in Figure S6 from Supplementary Material. The isotherms are Type IV, indicating adsorption on the mesoporous material (IUPAC classification). When the relative pressure ( $P/P_0$ ) is higher than 0.4, a hysteresis loop appears, indicating that capillary condensation occurs in the mesopores and macropores, with adsorption being dominated by capillary condensation and evaporation. At  $P/P_0 < 0.4$ , the adsorption and desorption isotherms coincide with each other, and the adsorption is dominated by van der Waals force at this stage. The N<sub>2</sub> adsorption-desorption curves differ from all of the reference values and are significantly affected by heating. Regarding the types of hysteresis loops, they can reflect pore morphology in the porous material. The hysteresis loop for all of the samples, except for the MX-80 bentonite, is between the H2 and H3 type, indicating the coexistence of ink bottle-like pores and many slit pores formed by the plate-shaped minerals [62]. For MX-80, the hysteresis loop is close to the H4 type, indicating the existence of slit-like pore produced by similar layered minerals. According to the modification of the hysteresis loop, all retrieved samples seem to increase the ink bottle-like pores.

Cation exchange capacity, CEC, is one of the most important parameters for characterising the bentonite adsorption behaviour. This parameter is equivalent to the total negative surface charge of a clay mineral and reflects the degree of reactivity of the bentonite because CEC is related to the capacity of adsorption and retention of ions and to the swelling capacity of the bentonites. The CEC parameter is linked with the interlayer cations, whose nature is also an important issue because the cation composition at exchange sites affects not only the exchange properties but also the plasticity, the swelling capacity and the rheological behaviour. Values of CEC and cation exchange population are observed in Figure 14 and Table S7 from the Supplementary Material. Slight but not significant variations are observed in CEC values with respect to initial values, slightly decreasing towards the heating source, except for the MX-80 bentonite block located at the bottom part. However, there is a complete readjustment in the cation exchange population in all bentonites. Na-bentonites (Asha 505 and MX-80) reduce their sodium content, increasing calcium. In the case of Mg-Ca bentonites (Rokle, Ibeco, FEBEX), sodium content increased, as well as the calcium content, and the higher the sodium increase content, the lower the initial sodium content at exchange sites in the bentonite (e.g., see Rokle with respect to FEBEX bentonite). Magnesium content tends to decrease in all samples, except in MX-80 bentonite, where values increase at the heater contact.

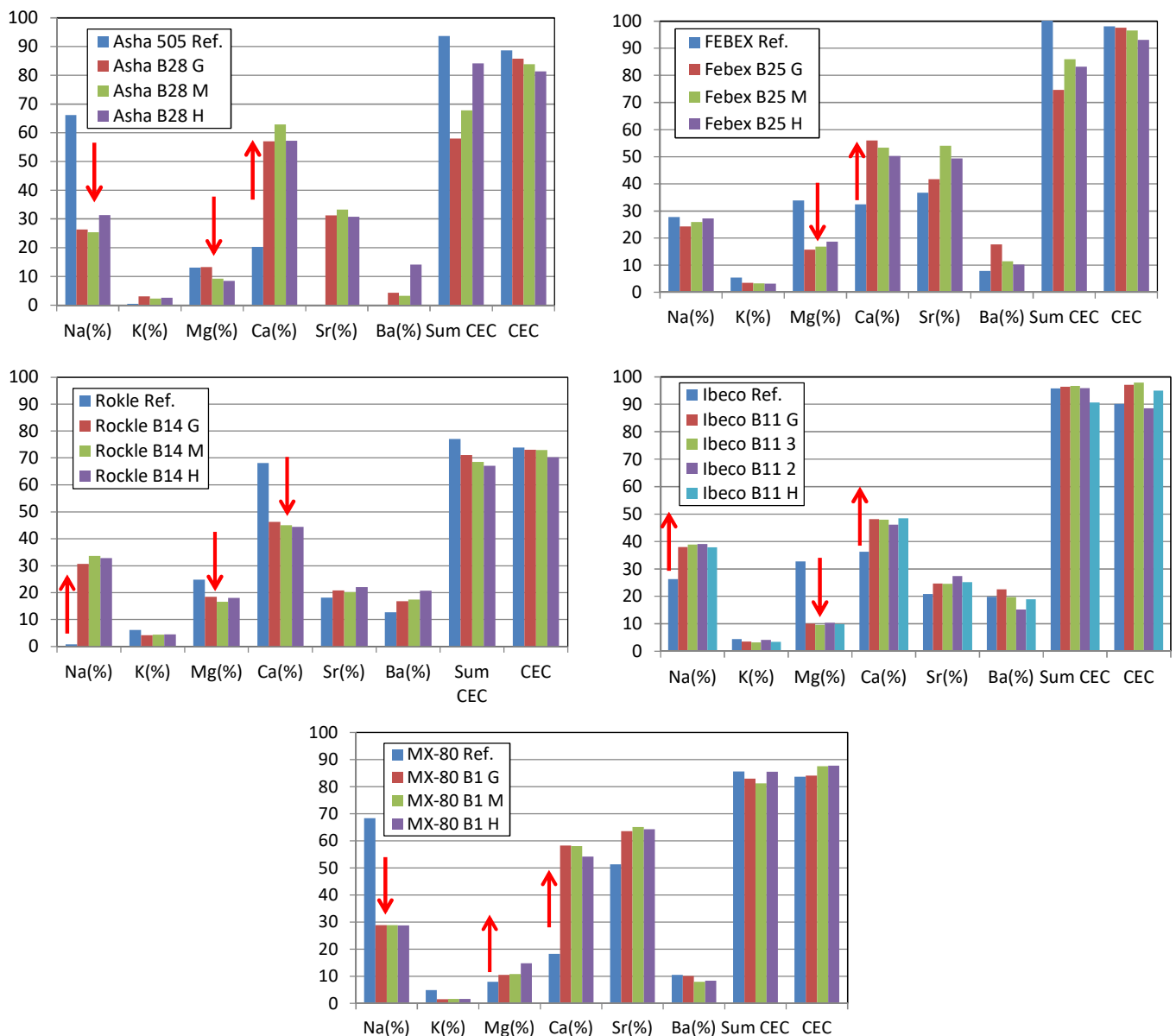


**Figure 14.** Cation exchange population after dismantling of the ABM5 experiment. Sr and Ba percentage is multiplied by 100 and 1000, respectively. Arrows: variations of content ( $\uparrow$ : increases or  $\downarrow$ : decreases).

Aqueous extracts were performed for obtaining ion inventories and ion distributions along the bentonite blocks (Tables S8 and S9 from Supplementary Material). It should be taken into account that only  $\text{Cl}^-$ ,  $\text{F}^-$ , and  $\text{Br}^-$  can be considered as conservative ions (only affected by anion exclusion phenomena), whereas the rest of the anions and cations are controlled by mineral dissolution/precipitation processes and ion exchange reactions during the leaching tests.

The soluble salts obtained from the samples taken after the ABM5 experiment are shown in Figure 15. The pH in the aqueous extracts is neutral with values between 7.6 and 7.8. Chloride values increased in all samples with respect to the initial reference values, but the content is lower at the heater contact (H) than at the granite contact (G), indicating a diffusion process through the compacted bentonite. It is interesting to see also the increased values of fluoride and bromide contents coming from the infiltrating Äspö groundwater (Table 2). Sulfate content depends on the type of bentonite and its

initial pore composition, although values increase towards the heater contact in most samples (Figure 16). Alkalinity values range between 0.3 and 0.7 mmol/100 g, expressed as  $\text{HCO}_3^-$ . Therefore, dissolution/precipitation processes of carbonates control the pH of the bentonites' pore water and cation exchange reactions. This is observed by cation content variations (Figure 16), which increased in all samples with respect to the reference samples, although with a tendency to decrease as a function of the heater contact, except for the Na-bentonites. Mg also increased at the heater contact in the Na-bentonites (Figure 16).

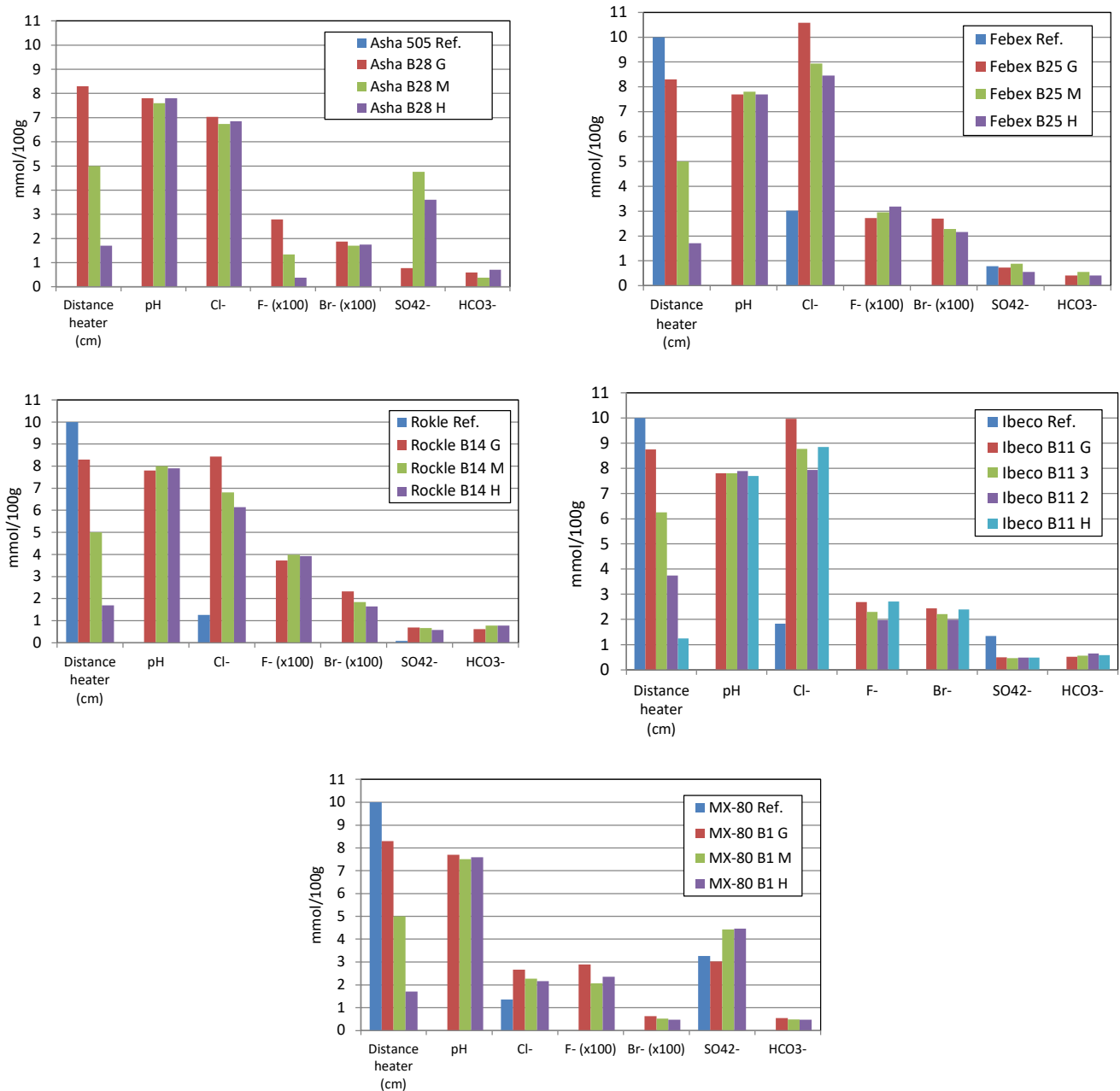


**Figure 15.** Anion distribution as a function of the heating contact obtained from leaching tests (in mmol/100 g). Reference data for chloride and sulfate are given for comparison.

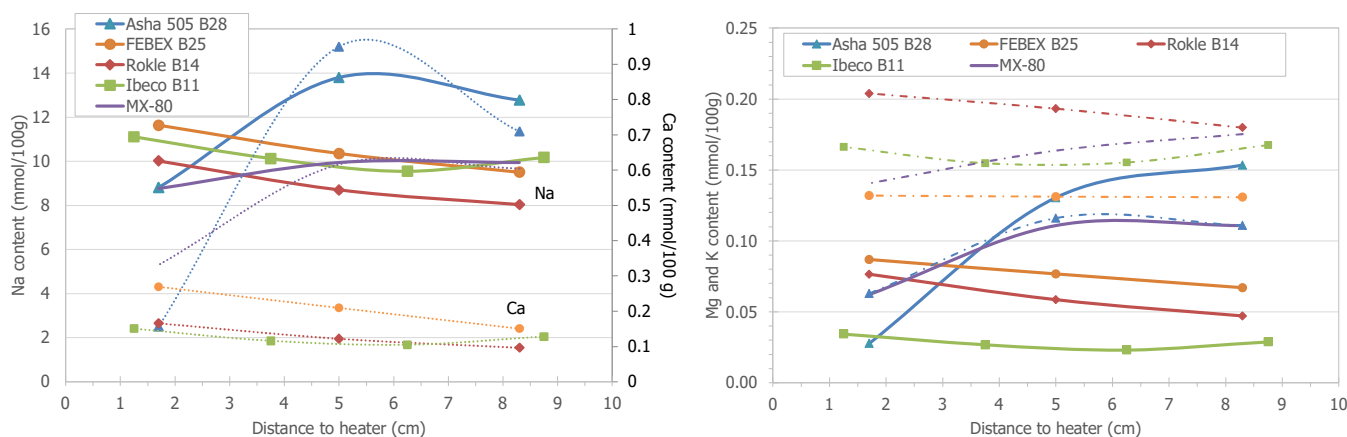


**Figure 16.** Cation distribution as a function of the heating contact obtained from leaching tests (in mmol/100 g). Reference data for chloride and sulfate are given for comparison.

### 3.5. Pore Water Chemistry

Pore water chemistry was obtained by squeezing at a pressure ranging between 20 and 30 MPa (Table 10), depending on the water content and dry density of the samples. The greater the water content of the sample, the lower the squeezing pressure that was needed (otherwise for dry density). The squeezing tests were performed with the pre-requirement of obtaining some amount of water enough for chemical analysis at the lowest squeezing pressure. This is because the greater the squeezing pressure, the greater the ease with which water bound to clay particle surfaces is expelled [38]. A representative pore water sample of homogeneously distributed electrolytes in the bulk aqueous phase requires avoiding the sampling of different portions of the diffuse layer water. Because of the high water content of the samples, pore water could be extracted at low squeezing pressures in a few days (3–7 days). It is worth noting that the whole piece of a bentonite block was used for squeezing tests, so the pore water chemical composition represents an average value from each bentonite block from the granite contact to the heater contact, in spite of there being a small solute gradient between these interfaces, as shown in Figures 15 and 16.

**Table 10.** Characteristics of the squeezing tests performed from bentonites after ABM5 dismantling.

Core Sample	Initial Mass (g)	Initial Dry Density (g/cm <sup>3</sup> )	Initial w.c. (%)	Time Elapsed (days)	Squeezing Pressure (MPa)	Pore Fluid Extracted/ Mass Loss (g)	Final Mass (g)	Final Dry Density (g/cm <sup>3</sup> )	Final w.c. (%)	Efficiency (%) <sup>(1)</sup>	Efficiency (%) <sup>(2)</sup>
Asha B28	208.74	1.53	28.6	7	20	7.3	201.44	1.62	26.4	45.3	15.7
FEBEX B25	369.23	1.49	26.6	7	30	10.1	359.15	1.62	24.8	58.8	13.0
Rokle B14	292.90	1.60	31.2	5	20	10.8	282.06	1.67	25.4	23.3	15.6
IBECO B11	187.07	1.49	36.0	3	20	7.1	180.00	1.55	28.7	49.5	14.3
MX-80 B1	201.08	1.51	35.8	3	30	5.8	195.26	1.60	25.9	17.2	11.0

<sup>(1)</sup> Efficiency (%) = (Collected water × 100)/Extracted water; <sup>(2)</sup> Total Efficiency (%) = (100 × extracted water)/(P<sub>initial</sub> − P<sub>dry</sub>).

The pH of the pore waters is neutral/slightly alkaline, with values ranging between 7.1 and 7.9 (Table 11). The salinity of the pore water is very high due to both the infiltrating marine Äspö groundwater (chloride content of 8580 mg/L (241.9 mmol/L, Table 2), and the high salinity of the initial bentonites pore water (Table S11 from Supplementary Material). After dismantling, ionic strength of pore waters ranges from 0.26 to 0.91 M, the lower values being at the bottom part of the bentonite column (MX-80 bentonite block 1).

**Table 11.** Chemical composition of the pore water extracted from the AMB5 bentonite blocks (n.d.: non determined).

Sample	Asha Block 28 S	FEBEX Block 25 W	Rokle Block 14 NW	IBECO Block 11 S	MX-80 Block 1 IN
Sq. Pressure (MPa)	20	30	20	20	30
Water content (%)	28.6	26.6	31.2	36.0	35.8
Total weight (g)	208.74	369.23	292.90	187.07	201.08
Water type	Na-Ca-Cl	Na-Ca-Cl	Na-Ca-Cl	Na-Ca-Cl	Na-Cl
pH	7.9	7.3	7.7	7.1	7.5
Alkalinity (meq/L)	0.94	0.90	0.90	0.76	1.18
F <sup>-</sup> (mg/L)	<1	<1	<1	<1	<1
Br <sup>-</sup> (mg/L)	152	195	128	112	28
Cl <sup>-</sup> (mg/L)	25,000	24,000	24,000	19,000	5800
SO <sub>4</sub> <sup>2-</sup> (mg/L)	1100	1100	1100	1700	1800
NO <sub>3</sub> <sup>-</sup> (mg/L)	6.1	<1	<1	3.3	1.3
Si (mg/L)	210	7.0	3.6	200	8.5
Al (mg/L)	<0.3	<0.3	0.08	<0.3	0.09
Na (mg/L)	9620	8100	9460	8040	3410
K (mg/L)	185	110	150	256	59
Ca (mg/L)	6100	4450	4350	3175	575
Mg (mg/L)	450	1500	560	850	180
Sr (mg/L)	49	60	47	30	12
Ba (mg/L)	0.45	0.52	0.55	<0.3	0.33
Fe (mg/L)	<0.3	1.4	<0.03	<0.3	0.04
Cu (mg/L)	0.67	0.70	0.39	1.0	0.19
B (mg/L)	4.5	0.90	0.26	3.1	0.07
Mn (mg/L)	1.3	2.8	0.52	8.9	0.59
Mo (mg/L)	<0.3	<0.3	0.37	<0.3	0.67
Ni (mg/L)	<0.3	1.7	0.14	3.9	2.0
Ti (mg/L)	<0.3	<0.3	<0.03	<0.3	<0.03
V (mg/L)	<0.3	<0.3	<0.03	<0.3	<0.03
Zn (mg/L)	0.41	<0.3	0.06	0.51	0.23
S <sub>2</sub> O <sub>3</sub> <sup>2-</sup> (mg/L)	<1	<1	<1	<1	<1
Acetate (mg/L)	51	<1	48	21	1.8
Formate (mg/L)	35	<1	2.0	741	14
TOC (mg/L)	n.d.	57.1	97.1	n.d.	44.2

The chemical composition of all bentonite pore waters is dominated by Cl<sup>-</sup>, Na and Ca, except for the more dilute pore water from MX-80 block 1, which is Na-Cl water type. The Äspö granitic groundwater (Ca-Na-Cl water type) is very saline with an ionic strength of 0.91 M (Table 2). During infiltration, the bentonite pore waters changes from mainly initial Na-Cl or Na-SO<sub>4</sub> water type (see Table S11 from Supplementary Material), towards a Na-Ca-Cl pore water in all bentonite blocks analysed, except for MX-80 block 1, which changes from Na-SO<sub>4</sub> to Na-Cl water-type.

Chloride concentration increased in all samples, with values ranging between 25,000 mg/L (705.2 mmol/L) and 5800 mg/L (163.6 mmol/L) from the top to the bottom of the bentonite package, with the lower values being located at the bottom part (MX-80 block 1). It should be taken into account the initial chloride contents of 6600, 2800 and 1100 mg/L for reference FEBEX, IBECO and MX-80 bentonites, respectively (Table S11 from Supplementary Material). The same behaviour occurs for Na and Ca, showing increased values.

Mg concentration in the pore water increased in all samples after the experiment, but variations depend on the initial composition of the bentonite pore water, being higher for the FEBEX bentonite [24,63] (Table S11). Sulfate contents are similar in all the bentonites, with concentrations ranging between 1100 and 1800 mg/L, and the higher values corresponding to Ibeco block 11 and MX-80 block 1 bentonites, which have higher initial reference values (4300 and 9300 mg/L, respectively, Table S11).

Alkalinity values are low, similar to that of the groundwater, with values ranging from 0.76 to 1.18 meq/L, and the highest value belonging to the MX-80 Block 1 pore water. However, these values seem to be much lower than those detected in reference samples (Table S11). It is interesting to note the presence of TOC, acetate, and formate in the pore waters (Table 11).

The geochemical code PHREEQC, version 3.4 [64] and the Thermoddem database [65] were used for equilibrium modelling and saturation indices calculations (Table S10 from Supplementary Material) at 25 °C. The saturation indices indicate that the pore waters from all samples are saturated with respect to calcite, gypsum, celestine, barite, calcite, dolomite, magnesite, barite and quartz (except Rokle) and undersaturated with respect to halite.

#### 4. Discussion

From the geochemical point of view, specific long-term requirements for the function of a bentonite to isolate the canisters from water and retard the migration of radionuclides is to maintain a suitable chemical environment for the canister integrity and radionuclide retention over time, buffering possible alteration/deterioration processes within the geological and engineered barrier systems. In this section, a discussion of results regarding the possible alterations of the bentonites after 4.4 years of the experiment is given.

##### 4.1. Physical Properties Variations

After 4.4 years of artificial hydration and heating, samples increased their water content by up to  $\sim 30 \pm 2\%$ , and the dry density decreased by up to  $\sim 1.52 \pm 0.05 \text{ g/cm}^3$  due to bentonite swelling capacity. Therefore, the total physical porosity increased from 29–39% to 45–48% of the compacted bentonite blocks after the infiltration of the saline groundwater (see microstructure of clay minerals Figure 9). Two factors probably influenced the mineralogical/geochemical behaviour in this experiment and the physico-chemical properties of the bentonites. First, due to the bentonite/groundwater infiltration and final salinity of the pore water, the relationship between external (pore water) and internal (interlayer water) must have been readjusted during the experiment due to the decrease in the thickness of the double diffuse layer (DDL), increasing the amount of available water (free water layer) for geochemical reactions. Second, the experiment was performed at a constant temperature of 50 °C during most of the experimental period (3.45 years). The temperature was increased to 150 °C for a period of 6 months and to 250 °C for the final 6 months (Figure 2). These final overheating periods probably provoked an impact on water distribution and final density, as observed after dismantling [8]. Dry density tends to increase towards the heating contact, indicating a collapse or shrinkage process of the clay minerals, which increases the inter-aggregate porosity and, hence, the external free water. Some micro-cracks are observed in samples at heater contact (e.g., Ibeco, MX-80 in Figure 3), and temperature increases the mineral dissolution. Both effects favour the increase in porosity. In addition, water content is higher at the bottom part of the bentonite package, in spite of supposed complete saturation of the bentonites. Indeed, the degree of saturation varies from 93 to 100% from the top to the bottom of the bentonite package probably due to steam–bentonite interactions which affected the bentonites/groundwater interactions. After dismantling, some geochemical modifications were observed depending on the location of the bentonite block inside the package. For example, calcite content in IBECO bentonite samples (Block 11) was drastically decreased, whereas calcite precipitation is observed in the bentonite blocks below and above. The variation in the sum of cation population and CEC values is not the same in samples located at the bottom part (IBECO block 11 and MX-80 Block 1) with respect to those located at the top part (Asha 505 Block 28, FEBEX Block 25 and Rokle block 14).

##### 4.2. Mineralogical and Geochemical Alterations

The high thermal conditions of this experiment (up to 250 °C) could have changed the bentonite clay minerals to non-swelling minerals, affecting the performance of the barrier.

However, there is no evidence for illitization, probably due to the low potassium contents both in pore water and exchange sites, despite the high temperatures. No modifications are observed in the clay mineral fraction after ethylene glycol treatment of the samples analysed (Figure 6).

In addition, metallic iron produced by corrosion of the heater could lead to [41]: (a) Fe(III) to Fe(II) reduction inside the clay mineral structure, affecting the layer charge, (b) dissolution/alteration of smectite to other minerals, and (c) cementation processes affecting plasticity, swelling or hydraulic conductivity of the bentonites. Trioctahedral smectites were found in previous experiments, such as the ABM1 and ABM2 experiments [6,12], the FEBEX *in situ* test [35,42], the TBT experiment [12], and the Prototype experiment [66]. However, in this work, no Mg- or Fe-rich trioctahedral smectites were detected despite the decrease in Mg at exchange sites and the increase in iron due to the corrosion of the C-steel heater. This is in agreement with other ABM5 studies [8,9]. Fully reducing conditions are important constraints for the alteration of dioctahedral smectites to trioctahedral ones.

The most interesting modifications found in the samples close to the heater were the increase in gypsum and calcite, and the presence of siderite, monohydrocalcite, pyrite and Na-clinoptilolite. These mineral phases decrease the porosity of the bentonite by means of a cementation process, and act as a sink of Fe(II), avoiding the modification of the clay mineral structure (e.g., transformation of montmorillonite to nontronite or saponite). However, not all of these mineral phases were found in all bentonites (Figure 5 and Table S1 from Supplementary Material). Goethite and hematite (due to heat), as the main Fe-oxides, and siderite were the corrosion products detected. Magnetite was not found (even by Mössbauer spectroscopy analysis) in spite of the increase in Fe(II) at the heater contact. Siderite neoformation was also observed in other ABM5 studies [8]. Hematite was not observed in all samples, only in Asha 505 Block 18, Rokle Block 14 and MX-80 Block 1. These bentonites contained higher amounts of goethite (Asha 505, Rokle) or siderite/pyrite (MX-80) in their reference samples. Precipitation of hematite may be due to heating (goethite to hematite transformation by heat), or due to siderite dissolution/pyrite oxidation in the case of MX-80. However, pyrite and siderite are still observed in all retrieved MX-80 samples analysed. Therefore, the presence of goethite or hematite may be related with a heater corrosion process under different oxic/anoxic environmental conditions, with the neoformation of goethite being favoured in presence of oxygen.

Dissolution/precipitation processes of calcite are observed, which seems to be affected by temperature and water vapour fluxes. Indeed, calcite dissolution increases with temperature. It is interesting to note the dissolution of calcite in the IBECO bentonite Block 11, which is not observed in the rest of the bentonite blocks located at the top and the bottom of the bentonite package, where an increase in carbonates is indicated. Monohydrocalcite is neoformed at the heater contact in Asha 505 bentonite. Gypsum content decreased in MX-80 bentonite Block 1 at heater contact but increased in Asha 505 Block 28. Anhydrite has not been found, although saturation indices from pore waters are oversaturated with respect to gypsum and anhydrite.

An increase in free silica can be ruled out, although an increase in tetrahedral charge in some clay minerals particles is observed. No significant variations in cristobalite/tridymite and feldspars mineral phases were found, although the intensity of their reflections increased in some samples.

#### 4.3. Redistribution of CEC and Exchangeable Cations

The cation composition at exchange sites for the different bentonites was modified after 4.4 years. Changes in exchangeable cation composition can be explained on the basis of equilibration with Äspo saline ( $I = 0.91$  M) groundwater (Table 2), which is enriched with Ca and Na salts, due to chemical interactions between the buffer blocks and temperature. The variation of the type of exchangeable cation in all bentonites seems to indicate that concentration tends to reach equilibrium with groundwater/pore water and tends to be

homogeneous in the whole bentonite column, with predominance of bivalent cations. However, complete equilibration of the cation occupancy was not achieved after 4.4 years of experiment due to the differences observed in the cation content at exchange sites and in the pore water chemistry both from the granite to the heater contact and from the top to the bottom of the column. The calcium bentonites increased their sodium content, and the sodium bentonites increased their calcium content, with exchangeable magnesium being replaced and decreased in all the samples, except in MX-80 block 1 located at the bottom of the column. In spite of the available and increased magnesium content in the pore water, no other additional magnesium-bearing mineral phases, such as saponite, were detected in the bentonites by SEM, XRD or FTIR (Table S1).

These cation exchange variations may involve the decrease in the external surface area noticed in all samples. This decrease may be explained by two mechanisms: (a) Missana et al. [67] showed that the presence of over 80% divalent cations at exchange sites favours the formation of large clay colloid particles, as well as that an increase in clay colloid size is produced when there is an increase in the tetrahedral charge, independently of the main interlayer cation. An increase in the particle size implies a decrease in the external surface area; (b) an increase in the electrolyte concentration affects the colloid properties (size and mobility) of the smectite due to the aggregation of clay particles. In this experiment, an increase in the size of clay particles is expected due to the increase in pore water salinity, divalent cations and the tetrahedral charge observed, favouring the decrease in the external surface area.

The CEC values seems to slightly decrease towards the heater contact from the upper part of the bentonite column towards the middle part (Asha 505 Block 28, FEBEX Block 25 and Rokle Block 14), with variations of  $-7.3$ ,  $5.0$  and  $-3.5$  meq/100 g in samples at the heater contact with respect to reference values. However, this decrease is not observed in the two blocks located at the bottom part of the column (IBECO block 11 and MX-80 Block 1), where changes are positive, increasing by about 4.5 meq/100 g.

The decrease in CEC at the heater contact has been observed in other *in situ* experiments [9,11,42,68,69]. The decrease in CEC values may be related to high-temperature conditions, water vapor formation [70], a lower content of smectite or to the decrease in the layer charge of the smectite clay particles. The smectite and total phyllosilicates contents in most of the samples are similar to the reference values, within the experimental error. Thus, other explanations need to be given. Interestingly, the sum of cations at exchange sites is similar to the total CEC value, except in the upper bentonite blocks (Asha 505 Block 28, FEBEX Block 25), where a decrease in exchangeable Mg was detected as an expense of an increase in exchangeable Ca. This observation was observed twice after repeating the determination, and also detected by [9]. The increase in calcium at exchange sites may be indicative of an increase in the calcite content in the retrieved samples, as observed in XRF data (Tables S3 and S4) and in [8], which could lead to its dissolution during the aqueous extraction. However, this should not affect the magnesium content at exchange sites, which decreases. Thus, this Mg decrease is not well understood.

A decrease in the CEC may be caused in this experiment by: (a) the collapse of clay particles, particularly of highly charged smectites [71], (b) the collapse of clay particles due to the high ionic strength of the pore water, reducing the swelling pressure (e.g., [18,72]), (c) extensive drying because of the increased Ca/Mg fixation and/or K fixation at interlayer sites [73]. All of these factors—the increase in layer charge, the increase in tetrahedral charge (Table 5), high salinity and drying—are implicated in this package system. These factors are controlled by temperature and water saturation. For this reason, the variations observed in the CEC parameter, decreasing at the top and increasing at the bottom of the bentonite column, seem to reflect that CEC is, in turn, affected by the temperature and water vapor fluxes.

#### 4.4. Pore Water Chemistry Variations

Intrinsic properties of bentonites, such as CEC, the presence of soluble minerals (e.g., calcite, gypsum, . . . ) and the low hydraulic conductivity and permeability of compacted material (i.e., solute transport by diffusion) imply a large buffering capacity for many geochemical processes. The chemical state of the buffer is defined by the bentonite composition (clay minerals and accessory minerals) and the pore water composition. Consequently, the chemical stability of the bentonite, that is, the alkalinity and redox buffering capacity, will be firstly controlled by the bentonite–water interactions and the resulting pore water chemistry (pH, redox potential, ionic strength, ionic composition, speciation and complexation). In addition, the knowledge of the porewater chemistry in the clay barrier is essential for performance assessment purposes in a nuclear waste repository, since the porewater composition controls the processes involved in the release and transport of the radionuclides.

In most studies performed with bentonites, it is observed that the bentonite composition controls the pore water chemistry evolution after their interaction with an infiltrating groundwater, and it is basically controlled by ion exchange reactions and dissolution/precipitation of the more soluble trace minerals of the bentonite [74–76]. However, this depends on the salinity of the infiltrating water, as observed in this experiment. In the case of the saline Äspö groundwater/bentonite interaction, the pore water chemistry depends on the diffusion rate of the infiltrating groundwater (which varies with the bentonite dry density and water content, i.e., porosity), and it is basically controlled by ion exchange and mineral dissolution/precipitation reactions.

The initial bentonite pore water was modified in all bentonite blocks after their interaction with the saline Na-Ca-Cl groundwater. However, the pore water composition is not at equilibrium in each bentonite block and in the whole bentonite package, since a diffusion infiltration process of the conservative ions ( $\text{Cl}^-$ ,  $\text{Br}^-$ ,  $\text{F}^-$ ) is still observed towards the heater after 4.4 years of the experiment. Anions diffuse more slowly than cations through the bentonite as a result of anion exclusion. Thus, a clear evolution of the pore water is observed after groundwater infiltration. The bentonite pore water changes from mainly initial Na-Cl or Na-SO<sub>4</sub> water-type (see Table S11 from Supplementary Material) towards Na-Ca-Cl pore water in all bentonite blocks analysed, except for MX-80 block 1, which changes from Na-SO<sub>4</sub> to Na-Cl water-type. The final ionic strength values of the pore waters (0.82–0.91 M) are similar in the upper bentonite blocks (Asha 505, FEBEX, Rokle) but lower at the bottom part of the package (IBECO and MX-80), with values of 0.69 and 0.26 M, respectively. Water vapor fluxes probably increased the salinity of the pore waters at the top part. However, variations in ion composition of the pore water indicate that pore water is controlled by the equilibration of infiltrating water with main accessory minerals and the exchanger (cation exchange sites and surface complexation sites). In any case, pore water chemistry data (Table 11) and anion inventory (Figure 15) indicate that saturated bentonites (including cation occupancy and pore water composition) are not at equilibrium with the external infiltrating groundwater. At each time, an equilibrium between pore water and exchange sites is established, but pore water chemistry is continuously modified during the diffusion transport of anions, which are affected by anion exclusion.

pH values are neutral in all pore water samples analysed, indicating the buffering capacity of the bentonite via protonation/deprotonation reactions and dissolution/precipitation of mainly calcite. Alkalinity values decreased in all samples and saturation indices from pore waters indicate saturated conditions with respect to calcite.

Organic matter (TOC) and acetate and formate (volatile fatty acids, VFAs) were found in pore water samples from the different bentonites (Table 11). At this interface, factors of temperature and possible hydrogen, available due to corrosion processes, may reflect the reduction of CO<sub>2</sub> to produce acetate and then formate, via abiotic or microbially induced reactions. However, the presence of microorganisms was not studied in this experiment and their implication in different reactions at the heater interface is a pure speculation. Another idea is that the hydrolysis of carbon-containing steels, leading to the generation of H<sub>2</sub>, CO<sub>2</sub>

and hydrocarbons, may be another possible process for the presence of acetate and formate in the pore water close to the heater, as discussed in [35,42]. Organics were not studied in this experiment, but their evolution should be taken into account in further studies.

#### 4.5. Iron–Bentonite Interactions

Metal corrosion was characterised by an increase in the Fe content in the samples and the presence of corrosion products, mainly close to the bentonite/heater interface. Most of the heater corrosion probably occurred in oxic conditions due to the observed corrosion products, goethite and hematite. However, oxygen may rapidly be depleted at the surface of steel by the reactions of Fe-bearing minerals in the bentonites: pyrite, siderite, Fe(II) in octahedral sites of montmorillonite particles, etc. However, this redox buffer capacity is limited due to the low amounts of reduced components, which will depend on the initial composition of each bentonite. In some zones, after oxygen depletion/consumption, the possible anoxic corrosion could produce some amount of Fe(II), which was transported by diffusion through the bentonite from the heater contact [14]. Indeed, an increase in Fe(II) is observed at the heater contact (Figures 11 and 13), with the content being much lower than Fe(III). This Fe(II) precipitated as siderite and pyrite, as shown by XRD in different samples (Figure 5), but not in all bentonites. Therefore, redox conditions must have been locally different. However, it seems that in this package system, oxygen is not completely depleted. Magnetite was not detected, in contrast to former ABM experiments [14]. In addition, variations in sulfur contents are insignificant.

## 5. Conclusions

Geochemical modifications of different bentonites (Asha 505, FEBEX, Rokle, IBECO and MX-80) used as engineered barriers were studied in the ABM5 experiment. In this medium large-scale *in situ* test, bentonite compacted blocks were artificially saturated with saline Äspö groundwater and heated progressively to 150 °C and finally up to 250 °C during the last six months.

The main change observed in all bentonites is the modification of exchangeable cation composition, explained on the basis of equilibration with Äspö saline groundwater enriched with Ca and Na salts. Calcium bentonites (FEBEX, Rokle, IBECO) increased their sodium content, and sodium bentonites (Asha 505, MX-80) increased their calcium content. Exchangeable magnesium decreased in all of the samples, except in MX-80 block 1 located at the bottom of the column. The variation of the type of exchangeable cations in all bentonites seems to indicate that concentration tends to reach equilibrium with groundwater/pore water and to be homogeneous in the whole bentonites column, with predominance of bivalent cations at exchange sites.

Cation exchange variations and/or salinity of the pore waters may explain the decrease in the external surface area values observed in all samples. However, swelling capacity is not affected due to the fact that the total surface area data are not modified.

A decrease in CEC values is observed towards the heating surface, which may be related to the high salinity of the pore water, a modification of the crystal structure of the smectite clay particles, increasing the layer charge, and the drying. These factors are driven by temperature, water vapor fluxes and water saturation.

In spite of the available and increased magnesium content in the pore water, no other additional magnesium-bearing mineral phases and/or trioctahedral smectites were detected, as found in ABM1 and ABM2 experiment. Furthermore, the transformation of montmorillonite to illite is discarded, probably due to the low potassium concentrations both in pore waters and exchange sites.

Fe increased as a function of the distance to the heater contact. Heater corrosion provoked the increase in iron in the bentonite, and goethite, hematite and siderite were found as corrosion products. No magnetite was detected. Although the ratio of ferrous to ferric iron increased in the close vicinity of the C-steel heater, the major Fe content is as Fe(III). No indications of Fe-montmorillonite were detected.

The initial bentonite pore water was modified in all bentonite blocks after their interaction with the saline Na-Ca-Cl groundwater. Pore waters changed from mainly an initial Na-Cl or Na-SO<sub>4</sub> water type towards a Na-Ca-Cl pore water in all bentonite blocks analysed, except for MX-80 block 1, which changes from Na-SO<sub>4</sub> to Na-Cl water-type. Water vapor fluxes probably increased the salinity of the pore waters at the top part of the package, since the final ionic strength (0.82–0.91 M) was similar in the upper bentonite blocks (Asha 505, FEBEX, Rokle) but lower in the bottom part of the package (IBECO and MX-80), with values of 0.69 and 0.26 M, respectively. The pore water chemistry of bentonites evolved as a function of the diffusion transport of the saline infiltrating groundwater (anions being affected by anion exclusion), the chemical equilibrium of cations at exchange sites and mineral dissolution/precipitation processes. These reactions are in turn dependent on temperature and water vapor fluxes. All bentonites preserved their hydro-geochemical properties, after being subjected to saline groundwater infiltration, heating and interaction with corroding metals during the 4.4 years of the experiment.

**Supplementary Materials:** The following are available online at <https://www.mdpi.com/article/10.3390/min12040471/s1>, Table S1. Mineral phases detected in the bentonite samples (by XRD, FTIR and SEM techniques); Table S2. Positions and assignments of vibrational bands of dioctahedral smectites, kaolinite and illite; Table S3. Chemical composition of the solid phase (total fraction) for different samples obtained after the dismantling of the ABM5 experiment: Asha Block 28, Febex Block 25 and Rokle Block 11; Table S4. Chemical composition of the solid phase (total fraction) for different samples obtained after the dismantling of the ABM5 experiment: Ibeco Block 11, MX-80 Block 1; Table S5. Fe(II), Fe(III) and total Fe contents obtained after the dismantling of the ABM5 experiment; Table S6. Parameters deduced from the BET and t-plot treatment on the adsorption of N<sub>2</sub> at 77 K from samples obtained after the dismantling of the ABM5 experiment, Table S7. Total cation exchange capacity (CEC) and cation exchange population prior to and after the dismantling of the ABM5 experiment (in meq/100 g); Table S8. Soluble salts from aqueous leaching tests a 1:4 solid to liquid ration, in mg/L; Table S9. Ion inventory obtained from aqueous leaching tests, in mol/100 g; Table S10. Calculated parameters and saturation indexes of the pore waters; Table S11. Chemical composition of the pore waters obtained by squeezing at 25 MPa for water vapour saturated FEBEX, IBECO RW C16, and MX-80 bentonites at initial conditions; Figure S1. XRD patterns of total fraction samples from ABM5 experiment; Figure S2. XRD patterns of oriented aggregate samples from ABM5 experiment (normal and after ethylene glycol and heating at 550 °C treatments); Figure S3. Wide scan XPS spectrum recorded from the sample Rokle 4H at heater contact, Figure S4. Fe 2p XPS spectra recorded from samples containing different concentrations of Fe(III) and Fe(II) standard compounds; Figure S5. Room temperature Mössbauer spectra recorded in a narrow range of velocities for Rokle samples: reference, 4H: close to the heater interface, 5M: middle, and 6G: close to granite interface, i.e., at 1.67 cm, 5.00 cm and 8.33 cm from heater contact, respectively, Figure S6. N<sub>2</sub> adsorption/desorption isotherms from reference and retrieved ABM5 samples.

**Author Contributions:** Conceptualization, A.M.F., J.F.M.; D.S. and P.S.; methodology, A.M.F., J.F.M. and D.S.; validation, A.M.F., J.F.M. and D.S.; formal analysis, A.M.F., J.F.M., D.S., P.N., F.J.L., L.M.R., M.Á.C., A.I.C. and S.F.; investigation, A.M.F.; P.N. and F.J.L., resources, CIEMAT, CSIC; data curation, A.M.F., J.F.M., D.S., P.N., F.J.L., L.M.R. and M.Á.C.; writing—original draft preparation, A.M.F.; writing—review and editing, A.M.F., J.F.M., D.S. and P.S. All authors have read and agreed to the published version of the manuscript.

**Funding:** This work was funded by the EURAD-Concord European Commission Project and CIEMAT. Financial support for grant RTI2018-095303-B-C51 funded by MCIN/AEI/10.13039/501100011033 and “ERDF A way of making Europe” is gratefully acknowledged.

**Data Availability Statement:** Not applicable.

**Acknowledgments:** We acknowledge to UCM (Madrid, Spain) and the Chemical Department from CIEMAT for performing the XRF, XRD, SEM and chemical analyses.

**Conflicts of Interest:** The authors declare no conflict of interest.

## References

1. Posiva SKB. Safety functions, performance targets and technical design requirements for a KBS-3V repository. Conclusions and recommendations from a joint SKB and Posiva working group. In *Posiva SKB Report 01*; Svensk Kärnbränslehantering AB: Stockholm, Sweden, 2017; p. 116.
2. Villar, M.V.; Armand, G.; Conil, N.; de Lesquen, C.; Herold, P.; Simo, E.; Mayor, J.C.; Dizier, A.; Li, X.; Chen, G.; et al. D7.1 HITEC. Initial State-of-the-Art on THM Behaviour of (i) Buffer Clay Materials and of (ii) Host Clay Materials. 2020. Deliverable D7.1 HITEC. EURAD Project, Horizon 2020 No 847593. 214p. Available online: <https://www.ejp-eurad.eu/sites/default/files/2021-04/EURAD%20-%20D7.1%20Initial%20SotA%20HITEC.pdf> (accessed on 7 April 2022).
3. Kaufhold, S.; Dohrmann, R. Distinguishing between more and less suitable bentonites for storage of high-level radioactive waste. *Clay Miner.* **2016**, *51*, 289–302. [[CrossRef](#)]
4. Dohrmann, R.; Kaufhold, S.; Lundqvist, B. The role of clays for safe storage of nuclear waste. In *Handbook of Clay Science*; Bergaya, F., Lagaly, G., Eds.; Elsevier: Amsterdam, The Netherlands, 2013; Volume 5B, pp. 677–710.
5. Svensson, D.; Sandén, T.; Olsson, S.; Dueck, A.; Eriksson, S.; Jägerwall, S.; Hansen, S. Alternative buffer material Status of the ongoing laboratory investigation of reference materials and test package 1. In *SKB TR-11-06*; Svensk Kärnbränslehantering AB: Stockholm, Sweden, 2011; p. 146.
6. Kaufhold, S.; Dohrmann, R.; Sandén, T.; Sellin, P.; Svensson, D. Mineralogical investigations of the first package of the alternative buffer material test—I. Alteration of bentonites. *Clay Miner.* **2013**, *48*, 199–213. [[CrossRef](#)]
7. Kaufhold, S.; Dohrmann, R.; Götze, N.; Svensson, D. Characterization of the second parcel of the Alternative Buffer Material (ABM) Experiment—I mineralogical reactions. *Clays Clay Miner.* **2017**, *65*, 27–41. [[CrossRef](#)]
8. Kaufhold, S.; Dohrmann, R.; Ufer, K.; Svensson, D.; Sellin, P. Mineralogical analysis of bentonite from the ABM5 heater experiment at Äspö hard rock laboratory, Sweden. *Minerals* **2021**, *11*, 669. [[CrossRef](#)]
9. Sudheer, K.R.; Podlech, C.; Grathoff, G.; Warr, L.N.; Svensson, D. Thermally induced bentonite alterations in the SKB ABM5 hot bentonite experiment. *Minerals* **2021**, *11*, 1017. [[CrossRef](#)]
10. Dohrmann, R.; Olsson, S.; Kaufhold, S.; Sellin, P. Mineralogical investigations of the first package of the alternative buffer material test—II. Exchangeable cation population rearrangement. *Clay Miner.* **2013**, *48*, 215–233. [[CrossRef](#)]
11. Dohrmann, R.; Kaufhold, S. Characterisation of the second package of the alternative buffer material (ABM) experiment—II Exchangeable cation population rearrangement. *Clays Clay Miner.* **2017**, *65*, 104–121. [[CrossRef](#)]
12. Svensson, P.D.; Hansen, S. Redox chemistry in two iron-bentonite field experiments at Äspö hard rock laboratory, Sweden: An XRD and Fe k-edge XANES study. *Clays Clay Miner.* **2013**, *61*, 566–579. [[CrossRef](#)]
13. Wersin, P.; Jenni, A.; Mäder, U.K. Interaction of corroding iron with bentonite in the ABM1 experiment at Äspö, Sweden: A microscopic approach. *Clays Clay Miner.* **2015**, *63*, 51–68. [[CrossRef](#)]
14. Wersin, P.; Hadi, J.; Jenni, A.; Svensson, D.; Grenèche, J.-M.; Sellin, P.; Leupin, O.X. Interaction of Corroding Iron with Eight Bentonites in the Alternative Buffer Materials Field Experiment (ABM2). *Minerals* **2021**, *11*, 907. [[CrossRef](#)]
15. Muurinen, A. *Studies on the Chemical Conditions and Microstructure in Package 1 of Alternative Buffer Materials Project (ABM) in Äspö*. Posiva Working Report; Posiva: Eurajoki, Finland, 2010; p. 39.
16. Sandén, T.; Nilsson, U.; Svensson, D. *ABM45 Experiment at Äspö Hard Rock Laboratory; Installation Report*; SKB Report P-18-20; Svensk Kärnbränslehantering AB: Stockholm, Sweden, 2018; p. 49.
17. Gordon, A.; Pahverk, H.; Börjesson, E.; Johansson, A.J. *Examination of Copper Corrosion Specimens from ABM45, Package 5*; Technical Report TR-18-17; Svensk Kärnbränslehantering AB: Stockholm, Sweden, 2018; p. 27.
18. Karnland, O.; Olsson, S.; Nilsson, U. *Mineralogy and Sealing Properties of Various Bentonites and Smectite-Rich Clay Materials*; SKB TR-06-30; Svensk Kärnbränslehantering AB: Stockholm, Sweden, 2006.
19. Slaughter, M.; Earley, J.W. *Mineralogy and Geological Significance of the Mowry Bentonites, Wyoming*; Special Paper N° 87; Geological Society of America: New York, NY, USA, 1965.
20. Christidis, G.; Scott, P.W.; Marcopoulos, T. Origin of the bentonite deposits of Eastern Milos, Aegean, Greece: Geological, Mineralogical and Geochemical Evidence. *Clays Clay Miner.* **1995**, *43*, 63–77. [[CrossRef](#)]
21. Konta, J. Textural variation and composition of bentonite derived from basaltic ash. *Clays Clay Miner.* **1986**, *34*, 257–265. [[CrossRef](#)]
22. Prikryl, R.; Woller, F. Going underground: A new market for Czech bentonite in nuclear waste disposal. *Ind. Miner.* **2002**, *415*, 72–77.
23. Huertas, F.; Farina, P.; Farias, J.; Garcia-Sineriz, J.L.; Villar, A.M.; Fernandez, A.M.; Martin, P.L.; Elorza, F.J.; Gens, A.; Sanchez, M.; et al. *FEDEX Project. Full-Scale Engineered Barriers Experiment for a Deep Geological Repository for High Level Radioactive Waste in Crystalline Host Rock*; Updated Final Report 1994-2004; Technical Publication ENRESA 5-0/2006; ENRESA: Madrid, Spain, 2006; p. 590.
24. Fernandez, A.M.; Baeyens, B.; Bradbury, M.; Rivas, P. Analysis of the pore water chemical composition of a Spanish compacted bentonite used in an engineered barrier. *Phys. Chem. Earth* **2004**, *29*, 105–118. [[CrossRef](#)]
25. Shah, N.R. Indian bentonite: Focus on the Kutch region. *Ind. Miner.* **1997**, *359*, 43–47.
26. Jackson, M.L. *Soil Chemical Analysis: Advanced Course*; Revised Second Edition; Parallel Press University of Wisconsin-Madison Libraries: Madison, WI, USA, 2005; p. 930.
27. Moore, D.; Reynolds, R. *X-ray Diffraction and the Identification and Analysis of Clay Minerals*; Oxford University Press: New York, USA, 1989; p. 332.

28. Newman, A.C.D. Chemistry of Clays and Clay Minerals. Mineral Society. Monograph N° 6. *Longman Sci. Tech.* **1987**, *6*, 480.
29. Wagner, C.D.; Davis, L.E.; Zeller, M.V.; Taylor, J.A.; Raymond, R.M.; Gale, L.H. Empirical atomic sensitivity factors for quantitative analysis by electron spectroscopy for chemical analysis. *Surf. Interface Anal.* **1981**, *3*, 211–225. [[CrossRef](#)]
30. Tarafder, P.K.; Thakur, R. An optimised 1,10-Phenanthroline method for the determination of ferrous and ferric oxides in silicate rocks, soils and minerals. *Geostand. Geoanal. Res.* **2012**, *37*, 155–168. [[CrossRef](#)]
31. Amman, L.; Bergaya, F.; Lagaly, G. Determination of the cation exchange capacity of clays with copper complexes revisited. *Clay Miner.* **2005**, *40*, 441–453. [[CrossRef](#)]
32. Sawhney, B.L. Potassium and caesium ion selectivity in relation to clay mineral microstructure. *Clays Clay Miner.* **1970**, *18*, 47–52. [[CrossRef](#)]
33. Gregg, S.J.; Sing, K.S.W. *Adsorption, Surface area and Porosity*; Academic Press: London, UK, 1982; p. 303.
34. Keeling, P.S.; Kirby, E.C.; Robertson, R.H.S. Moisture adsorption and specific surface area. *J. Brit. Ceram. Soc.* **1980**, *79*, 36–40.
35. Fernández, A.M.; Sánchez-Ledesma, D.M.; Melón, A.; Robredo, L.M.; Rey, J.J.; Labajo, M.; Clavero, M.A.; Fernández, S.; González, A.E. *Thermo-Hydro-Chemical (THC) Behaviour of a Spanish Bentonite after Dismantling Heater#1 and Heater#2 of the FEBEX In Situ Test at the Grimsel Test Site*; Nagra Working Reports. NAB 16-25; Nagra: Wettingen, Switzerland, 2018; p. 583.
36. Fernández, A.M.; Bath, A.; Waber, H.N.; Oyama, T. Annex 2: Water sampling by squeezing drillcores. In *Geochemistry of Water in the Opalinus Clay Formation at the Mont Terri Rock Laboratory*; Pearson, F.J., Arcos, D., Bath, A., Boisson, J.Y., Fernández, A.M., Gäbler, H.-E., Gaucher, E., Gautschi, A., Griffault, L., Hernán, P., et al., Eds.; Geology Series No. 5; Federal Office for Water and Geology (FOGW): Bern, Switzerland, 2003; pp. 171–199.
37. Fernández, A.M. Caracterización y Modelización del Agua Intersticial en Materiales Arcillosos: Estudio de la Bentonita de Cortijo de Archidona. Ph.D. Thesis, CIEMAT, Madrid, Spain, 2004; p. 505.
38. Fernández, A.M.; Sánchez-Ledesma, D.M.; Tournassat, C.; Melón, A.; Gaucher, E.C.; Astudillo, J.; Vinsot, A. Applying the squeezing technique to highly consolidated clayrocks for pore water characterisation: Lessons learned from experiments at the mont terri rock laboratory. *Appl. Geochem.* **2014**, *49*, 2–21. [[CrossRef](#)]
39. Entwisle, D.C.; Reeder, S. New apparatus for pore fluid extraction from mudrocks for geochemical analysis. In *Geochemistry of Clay-Pore Fluid Interactions*; The Mineralogical Society Series; Chapman and Hall: London, UK, 1993; pp. 365–388.
40. Peters, C.A.; Yang, Y.C.; Higgins, J.D.; Burger, P.A. A preliminary study of the chemistry of pore water extracted from tuff by one-dimensional compression. In *Water-Rock Interaction*; Kharaka, Y.K., Maes, A.S., Eds.; A.A.Balkema: Rotterdam, The Netherlands, 1992; pp. 741–745.
41. Svensson, D. The Bentonite Barrier. Swelling Properties, Redox Chemistry and Mineral Evolution. Ph.D. Thesis, Lund University, Lund, Sweden, 2015.
42. Fernández, A.M.; Kaufhold, S.; Sánchez-Ledesma, D.M.; Rey, J.J.; Melón, A.; Robredo, L.M.; Fernández, S.; Labajo, M.A.; Clavero, M.A. Evolution of the THC conditions in the FEBEX *In Situ* test after 18 years of experiment: Smectite crystallochemical modifications after interactions of the bentonite with a C-steel heater at 100 °C. *Appl. Geochem.* **2018**, *98*, 152–171. [[CrossRef](#)]
43. War, L. IMA–CNMNC approved mineral symbols. *Mineral. Mag.* **2021**, *85*, 291–320. [[CrossRef](#)]
44. Alburquenque, D.; Márquez, P.; Troncoso, L.; Pereira, A.; Celis, F.; Sánchez-Arenillas, M.; Marco, J.F.; Gautier, J.L.; Escrig, J. LiM<sub>0.5</sub>Mn<sub>1.5</sub>O<sub>4-δ</sub> (M = Co or Fe) spinels with a high oxidation state obtained by ultrasound-assisted thermal decomposition of nitrates. Characterization and physicochemical properties. *J. Solid State Chem.* **2020**, *284*, 121175. [[CrossRef](#)]
45. López, G.P.; Castuer, D.G.; Ratner, B. XPS 0 1s Binding Energies for Polymers Containing Hydroxyl, Ether, Ketone and Ester Groups. *Surf. Interf. Anal.* **1991**, *17*, 267–272. [[CrossRef](#)]
46. Marco, J.F.; Gancedo, J.R.; Ortiz, J.; Gautier, J.L. Appl. Characterization of the spinel-related oxides Ni<sub>x</sub>Co<sub>3-x</sub>O<sub>4</sub> (x=0.3,1.3,1.8) prepared by spray pyrolysis at 350 °C. *Surf. Sci.* **2004**, *227*, 175–186. [[CrossRef](#)]
47. Smirnov, M.Y.; Kalinkin, A.V.; Bukhtiyarov, V.L. X-ray photoelectron spectroscopic study of the interaction of supported metal catalysts with NO<sub>x</sub>. *J. Struct. Chem.* **2007**, *48*, 1053–1066. [[CrossRef](#)]
48. Meskinis, S.; Vasiliauskas, A.; Androlevicius, M.; Peckus, D.; Tamulevicius, S.; Viskontas, K. Diamond Like Carbon Films Containing Si. *Struct. Nonlinear Opt. Prop. Mater.* **2020**, *13*, 1003.
49. Bancroft, G.M. *Mössbauer Spectroscopy: An Introduction for Inorganic Chemists and Geochemists*; McGraw Hill: Maidenhead, UK, 1973.
50. Maddock, A.G. Mössbauer Spectrometry in Mineral Chemistry. In *Chemical Bonding and Spectroscopy in Mineral Chemistry*; Berry, F.J., Vaughan, D.J., Eds.; Springer: Berlin/Heidelberg, Germany, 1985; pp. 141–208.
51. Coey, J.M.D. Clay minerals and their transformations studied with nuclear techniques: The contribution of Mössbauer spectroscopy. *At. Energy Rev.* **1980**, *18*, 73–124.
52. Heller-Kallai, L.; Rozenson, I. The use of Mössbauer spectroscopy of iron in clay mineralogy. *Phys. Chem. Miner.* **1981**, *7*, 223–238. [[CrossRef](#)]
53. De Grave, E.; Vandenbruwaene, J.; Elewaut, E. An<sup>57</sup>Fe Mössbauer effect study on glauconites from different locations in Belgium and northern France. *Clay Miner.* **1985**, *20*, 171–179. [[CrossRef](#)]
54. Dainyak, L.G.; Drits, V.A. Interpretation of Mössbauer spectra of nontronite, celadonite and glauconite. *Clays Clay Miner.* **1987**, *35*, 363–373. [[CrossRef](#)]
55. Dainyak, L.G.; Drits, V.A.; Heifits, L.M. Computer simulation of cation distribution in dioctahedral 2:1 layer silicates using IR-data: Application to Mössbauer spectroscopy of a glauconite sample. *Clays Clay Miner.* **1992**, *40*, 470–479. [[CrossRef](#)]

56. Pelayo, M.; Marco, J.F.; Fernández, A.M.; Vergara, L.; Melón, A.M.; del Villar, L.P. Infrared and Mössbauer spectroscopy of Fe-rich smectites from Morrón de Mateo bentonite deposit (Spain). *Clay Miner.* **2018**, *53*, 17–28. [[CrossRef](#)]
57. Murad, E.; Johnston, J.H. *Iron Oxides and Oxyhydroxides. Mössbauer Spectroscopy Applied to Inorganic Chemistry*; Gary, J., Ed.; Plenum Press: New York, NY, USA, 1987; Volume 2, Chapter 12; pp. 507–582.
58. Vandenberghe, R.E.; De Grave, E. Application of Mössbauer spectroscopy in earth sciences. In *Mössbauer Spectroscopy. Tutorial Book*; Yoshida, Y., Langouche, G., Eds.; Springer: Berlin/Heidelberg, Germany, 2013; Chapter 3; pp. 91–186.
59. Dang, M.Z.; Rancourt, D.G.; Dutrizac, J.E.; Lamarche, G.; Provencher, R. Interplay of surface conditions, particle size, stoichiometry, cell parameters, and magnetism in synthetic hematite-like materials. *Hyperfine Interact.* **1998**, *117*, 271–319. [[CrossRef](#)]
60. Goss, C.J. The kinetics and reaction mechanism of the goethite to hematite transformation. *Mineral. Mag.* **1987**, *51*, 437–451. [[CrossRef](#)]
61. Hernández, T.; Sánchez, F.J.; Morono, A.; Aristu, M.; Marco, J.F. Effect of irradiation on the stability of the corrosion layer produced in Eurofer by contact with lithium ceramics. *J. Nucl. Mater.* **2021**, *545*, 152614. [[CrossRef](#)]
62. Sing, K.S.W.; Everett, D.H.; Haul, R.A.W.; Moscou, L.; Pierotti, R.A.; Rouquerol, J.; Siemieniewska, T. Reporting physisorption data for gas/solid systems with Special Reference to the Determination of Surface Area and Porosity. *Pure Appl. Chem.* **1985**, *57*, 603–619. [[CrossRef](#)]
63. Fernández, A.M.; Rivas, P. Pore water chemistry of saturated Febex bentonite compacted at different densities. In *Advances in Understanding Engineered Clay Barriers*; Alonso, E.E., Ledesma, A., Eds.; Balkema Publishers: Leiden, The Netherlands, 2005; pp. 505–514.
64. Parkhurst, D.L.; Appelo, C.A.J. Description of input and examples for PHREEQC version 3—A computer program for speciation, batch-reaction, one-dimensional transport, and inverse geochemical calculations: U.S. In *Geological Survey Techniques and Methods*; U.S. Geological Survey: Denver, CO, USA, 2003; Chapter A43; p. 497.
65. Blanc, P. *Thermodem: Update for the 2017 Version*; Report BRGM/RP-66811-FR; BRGM: Orleans, France, 2017; p. 20.
66. Olsson, S.; Jensen, V.; Johansson, L.E.; Hansen, E.; Karnland, O.; Kumpulainen, S.; Kirivanta, L.; Svensson, D.; Hansen, S.; Lindén, J. *Prototype Repository-Hydromechanical, Chemical and Mineralogical Characterization of the Buffer and Backfill Material from the Outer Section of the Prototype Repository*; Technical Report TR-13-21; Svensk Kärnbränslehantering AB: Stockholm, Sweden, 2013.
67. Missana, T.; Alonso, U.; Fernández, A.M.; García-Gutiérrez, M. Analysis of the stability behaviour of colloids obtained from different smectite clays. *Appl. Geochem.* **2018**, *92*, 180–187. [[CrossRef](#)]
68. Kaufhold, S.; Dohrmann, R.; Ufer, K.; Kober, F. Interactions of bentonite with metal and concrete from the FEBEX experiment—mineralogical and geochemical investigations of selected sampling sites. *Clay Miner.* **2018**, *53*, 745–763. [[CrossRef](#)]
69. Dohrmann, R.; Kaufhold, S. Cation exchange and mineral reactions observed in MX 80 buffer samples from the Prototype repository *in situ* experiment in Äspö, Sweden. *Clays Clay Miner.* **2014**, *5*, 357–373. [[CrossRef](#)]
70. Heuser, M.; Weber, C.; Stanjek, H.; Chen, H.; Jordan, G.; Schmahl, W.W.; Natzeck, C. The interaction between bentonite and water vapor. I: Examination of physical and chemical properties. *Clays Clay Miner.* **2014**, *62*, 188–202. [[CrossRef](#)]
71. Kaufhold, S.; Dohrmann, R. Stability of bentonites in salt solutions: II. Potassium chloride solution. Initial step of illitization? *Appl. Clay Sci.* **2010**, *49*, 98–107. [[CrossRef](#)]
72. Herbert, H.-J.; Kasbohm, J.; Sprenger, H.; Fernández, A.M.; Reichelt, C. Swelling pressures of MX-80 bentonite in solutions of different ionic strength. *Phys. Chem. Earth* **2008**, *33*, 327–342. [[CrossRef](#)]
73. Kaufhold, S.; Dohrmann, R. Effect of extensive drying on the cation exchange capacity of bentonites. *Clay Miner.* **2010**, *45*, 441–448. [[CrossRef](#)]
74. Fernández, A.M.; Cuevas, J.; Rivas, P. Pore water chemistry of the FEBEX bentonite. *Mat. Res. Soc. Symp. Proc.* **2001**, *663*, 573–588. [[CrossRef](#)]
75. Wersin, P. Geochemical modelling of bentonite pore water in high-level waste repositories. *J. Contam. Hydrol.* **2003**, *61*, 405–422. [[CrossRef](#)]
76. Bradbury, M.H.; Berner, U.; Curti, E.; Hummel, W.; Kosakowski, G.; Thoenen, T. *The Long Term Geochemical Evolution of the Nearfield of the HLW Repository*; Nagra Technical Report NTB 12-01; NAGRA: Wettingen, Switzerland, 2014.